Icarus 237 (2014) 388–414

Contents lists available at ScienceDirect

Icarus

journal homepage: www.elsevier.com/locate/icarus

Atmospheric mesoscale modeling of water and clouds during northern summer on Mars

Daniel Tyler Jr. *, Jeffrey R. Barnes

College of Earth Oceanic and Atmospheric Science, Oregon State University, Corvallis, OR 97331, United States

ARTICLE INFO

Article history:
Received 30 September 2013
Revised 11 March 2014
Accepted 16 April 2014
Available online 26 April 2014

Keywords:
Atmospheres, dynamics
Mars, climate
Mars, polar caps
Mars, atmosphere
Meteorology

ABSTRACT

For a key season in the annual water cycle ($L_s \sim 120°$) a mesoscale model is used to study atmospheric water vapor and water ice clouds in the northern polar region of Mars. Model results at high-resolution (15 km) allow the examination of various mesoscale aspects of the circulation in this complex (topography, albedo and thermal inertia) region. A simple cloud scheme is used, where only the mean cloud particle size is carried, and nucleation is not explicitly treated. For this study, new high-resolution maps of albedo and thermal inertia were developed (poleward of 60°N), and model ground temperatures are in good agreement with observations at high resolution, typically within ~5 K of TES (for ice and non-ice locations at AM and PM times of day). Diurnal mean sublimation rates are greatest along the edges of the polar dome and the largest outliers (~25–50 μm/sol). This is a consequence of widespread stability (atmospheric inversion) over the cold interiors of the largest ice surfaces, as well as strong ventilating winds that are modeled around the polar dome with sufficient spatial resolution. The structure of high latitude atmospheric water vapor is complex, especially so near Phoenix. Dynamically, two factors are responsible: (1) the transient circulations that form in the baroclinic zone around the polar dome and (2) a "storm zone" that forms on the poleward slopes of Alba Patera where there is additional transient activity that has a sizeable effect on the Phoenix region. This "storm zone" forms because of a rapidly evolving aspect of the regional circulation, and it plays a key role in the seasonally recurring annular cloud (that is simulated in this study). Also simulated are observations made during the Phoenix mission that seem to be dynamically related to the appearance of the annular cloud. Together this may signify a seasonal transition in the region. To simulate realistic clouds over the polar region (compared with opacity observations and imagery), a sufficiently realistic circulation appears to be important, and relatively high spatial resolution is needed for this. If a low-resolution run (135 km, no nests) is compared to a high-resolution run (two levels of nesting to 15 km in the polar region), we find that the high-resolution case produces ten times less cloud ice over the most polar latitudes. The activation of the first nest (45 km) produces a sufficiently realistic circulation, such that excess vapor and cloud ice are readily ventilated equatorward from polar latitudes. A more sophisticated cloud scheme might serve to reduce the sensitivity seen in this study. However, sufficient spatial resolution is what causes the circulation to become realistic, and in this regard microphysics is not involved.

1. Introduction

The North Polar Layered Deposits and the outlier ices are believed to be the primary sources of atmospheric water in the present-day water cycle on Mars. These permanent (residual) ices play a key role in the annual water cycle; hereafter they will be collectively referred to as the North Polar Residual Cap (NPRC). In the absence of seasonal CO_2 frost deposits, the NPRC region is extremely complex, with dramatic and fine-scale transitions between bright and dark surfaces (ices and/or regolith/fines). The topography of the region itself is highly complex. Moreover, since fine-scale changes in surface type lead to very sharp gradients in ground temperature, strong smaller-scale circulations must have an important role in the regional circulation. For any season, mesoscale models are powerful tools for studying the various circulations in the NPRC region. When a mesoscale model is carefully configured for the season of interest, high-resolution simulations will provide a realistic depiction of circulations over a very wide

* Corresponding author.
E-mail addresses: dtyler@coas.oregonstate.edu (D. Tyler Jr.), barnes@coas.oregonstate.edu (J.R. Barnes).

http://dx.doi.org/10.1016/j.icarus.2014.04.020
0019-1035/

range of scales. In an analysis of the results from such simulations, subtle aspects of the water cycle can be understood more completely, a primary and long-term goal of this work.

Global Climate Models (GCMs), which simulate the interactions over the entire planet between atmospheric dynamics and microphysical water processes, are themselves extremely important tools. GCMs have greatly benefited our understanding of atmospheric circulations and the water cycle on Mars (e.g., Houben et al., 1997; Richardson and Wilson, 2002; Montmessin et al., 2004; Bottger et al., 2005). Regarding the present-day water cycle, GCM studies often consider two unresolved issues: (1) whether the NPRC is gaining or losing ice mass and (2) whether the high latitude regolith is an important source/sink term in the annual water cycle. In general, GCMs are capable of producing good agreement with the observed water cycle. However, due to the fine-scale complexity of the polar region, a typically configured GCM (with at best a spatial resolution of a few degrees, that is subject to the "pole problem" – a meridionally stretched grid in polar latitudes that requires non-physical filtering to maintain computational stability) simply cannot resolve the smaller-scale circulations. These smaller-scale circulations may be very important. When GCM results are compared with observations of summertime clouds, discrepancies are typically seen. GCMs tend to simulate water ice clouds that are too thick (Haberle et al., 2011; Madeleine et al., 2011, 2012). It is possible that a large part of the reason for this is that GCMs cannot realistically simulate the net effect of all the important subgrid circulations in the northern polar summertime atmosphere. To study this specific issue, mesoscale modeling can be used to refine our understanding, which will eventually lead to a more quantitative study of the subtle scientific questions regarding the water cycle.

When mesoscale models are configured with multiple levels of nesting over a location of interest, the circulation is simulated over a very large part of the planet, and also for some specific region at very high resolution (often to ~5 km or better). In this study, the specific season/region of interest is northern polar summertime and the exposed NPRC ices. When configured on a polar stereographic projection, model dynamics are not subject to the "pole problem", and non-physical filtering is not required. Mesoscale models cannot be run like GCMs (where a number of years are simulated for the entire planet in a single run). This is primarily due to the two penalties of increased resolution: (1) computational expense grows with higher resolutions because shorter timesteps are required and (2) computational expense grows with the far greater number of locations that are carried in a simulation. However, if the model is carefully configured, the results are highly complementary to those from a GCM over a narrow seasonal range. In comparing results over a sufficiently long period (when the same GCM is typically being used to provide boundary and initial conditions), the cumulative effect of smaller-scale circulations in the atmosphere can be investigated. If, when averaged to the GCM resolution, the mesoscale model results are in good agreement with the GCM, it is reasonable to conclude that the GCM is performing in a sufficiently realistic way at a much lower resolution. If not, additional analysis is required to investigate the underlying causes, which may lead to the development of GCM parameterizations that account for unresolved circulations. In lieu of a comprehensive set of atmospheric observations, this approach becomes a very important role for mesoscale models, and the issue of excessive cloudiness in the polar northern summertime is an appropriate problem.

In this work we focus on $L_s \sim 120°$. This season is very important in the annual water cycle, as well as good for beginning these investigations. As described by Smith (2002), the global and northern hemisphere atmospheric water vapor abundances are at annual maxima, while the transition into typical northern winter circulation patterns does not begin until later, $L_s \sim 150°$ (Tyler and Barnes, 2005). In fact, $L_s \sim 120°$ is a season of very small trends, which makes it useful for investigating how a mesoscale model performs, especially for understanding the simulation time that is required to "spin up" from low-resolution GCM initial conditions to an equilibrium between microphysics, dynamics and transport processes at the higher resolution of the mesoscale model. During this season, the NPRC is entirely free of seasonal CO_2 frost, and lateral GCM boundary conditions are entirely responsible for any change in the mass of the atmosphere. High latitude albedo values are not subject to much change at this season, and the values are fairly well known and represented in the data (Wendy Calvin, personal communication, 2009). Observations of clouds by the LIDAR on Phoenix (Whiteway et al., 2009), surface pressure, surface winds, surface air temperatures and imagery during this season are invaluable data for examining model performance. More can be understood with observations that are simultaneous (Tamppari et al., 2010). Additionally, the Thermal Emission Spectrometer (TES) observations (air and ground temperatures, and opacity data for both dust and ice) are central in model tuning and in providing benchmarks for comparison with model results.

2. The OSU Mars mesoscale model

The Oregon State University Mars Mesoscale Model (OSU MMM, Tyler et al., 2002) has been used in studies of atmospheric dynamics in the northernmost latitudes of Mars from late spring through late summer (Tyler and Barnes, 2005; Tyler et al., 2008). Since these earlier studies, two modifications have been made that significantly improve model performance in comparison to observations of atmospheric temperature.

The first is that atmospheric dust now varies with latitude. In an approach that is somewhat different from the way dust is typically treated in GCMs, the column dust opacity is prescribed at the zonal-mean surface pressure (not at the 6.1 mbar level). The meridional profile of opacity is based on the zonal-mean of the mapped TES infrared column opacity data (Smith et al., 2001). The opacity profile is modified a small amount to tune model temperatures towards a better agreement with TES observations. It is valid for a specific date ($L_s = 120°$) and remains constant during the simulation. The depth of the well-mixed layer above the ground (feature of the Conrath-Nu vertical dust prescription) is more realistic over the entire planet when keyed to the zonal-mean surface pressure instead of the 6.1 mbar level. This also allows shallow dust layers to be prescribed over high northern latitudes (where the 6.1 mbar surface is too far above the ground). The opacity of dust at the surface varies with longitude according to the difference between the local surface pressure and the zonal-mean surface pressure; if the local surface pressure is greater than the zonal-mean value, the mixing ratio of dust is held constant at the appropriate value for the zonal-mean surface pressure. The dust distribution that is used in this study is shown in Fig. 1.

The second modification is to the Rayleigh Friction (RF) layer at the top of the model atmosphere. The strength and depth of RF are now prescribed as a function of latitude and season. In developing this approach, we found that it can significantly improve model agreement with observations at high latitudes in the winter hemisphere, where Mars Climate Sounder (MCS) revealed the existence of sizeable polar warmings (McCleese et al., 2007). The use of variable RF is a crude way to parameterize the influence of breaking gravity waves, which presumably play an important role in the observed polar warmings. Since the lateral boundary of the mother domain of the mesoscale model reaches fairly deep into the southern hemisphere (the mother domain is polar stereographic and semi-global), RF is prescribed identically in the version of the NASA

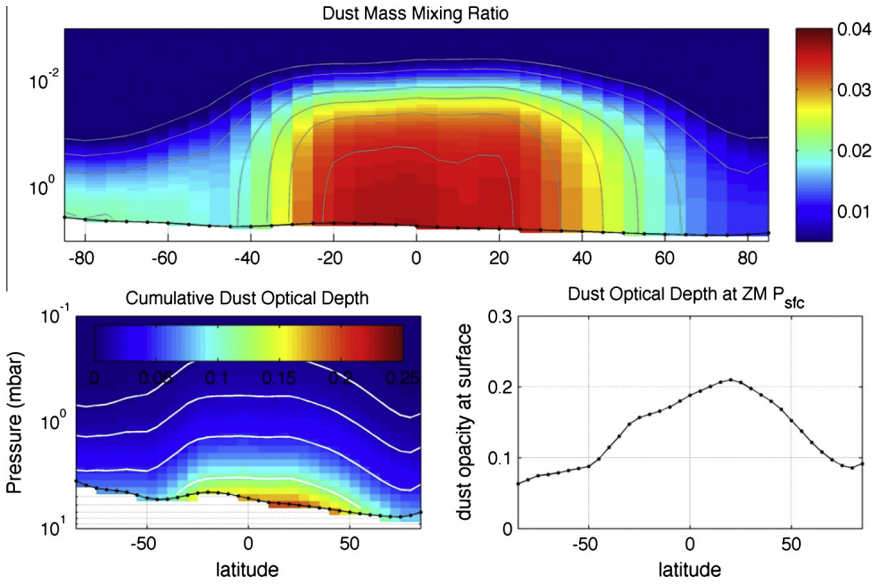

Fig. 1. The $L_s \sim 120°$ dust prescription is shown. The visible opacity of dust in the atmosphere is prescribed. This prescription is used in both the Ames GCM and the OSU MMM for all simulations in this study. The column opacity shown in the lower right subplot is prescribed at the zonal-mean surface pressure (not at the 6.1 mbar level).

Ames GCM (Kahre et al., 2006) that is being used for boundary and initial conditions. Together, these changes provide a more realistic lateral boundary for the mother domain, which is important when the edge of the seasonal CO_2 frost deposits is near its most northern reach at $L_s \sim 120°$.

2.1. Boundary and initial conditions, and two-way nesting

Boundary and initial conditions come from a version of the NASA Ames GCM (Kahre et al., 2006) that is maintained at OSU. The GCM is run in a seasonal configuration with three modifications: (1) seasonal CO_2 cap edges are prescribed as in the OSU MMM, based on the work of Titus (2005), (2) the total column visible dust opacity is prescribed as in the OSU MMM (see text above), and (3) RF is prescribed in the same way as in the OSU MMM (see text above). The GCM is run for a total of 60 sols; the first 30 are discarded to model spin-up and the final 20 are centered on the period of this study, $L_s = 120°$. Running the GCM this way allows for multiple run (iterative) tuning to observations, such as to the VL1 surface pressure record or to atmospheric temperature data from TES or MCS. The GCM surface pressure (at VL1) is compared with VL1 observations in Fig. 2, which shows that both the trend and magnitude are well matched.

Using 20 sols of results centered on $L_s = 120°$, the time/zonal-mean air temperatures from both the Ames GCM and the OSU MMM are compared in Fig. 3 with an average of the TES AM and PM temperatures. The GCM used in this study does not have Radiatively Active Clouds (RAC), nor does the OSU MMM. Because of this, the warmer temperatures observed by TES at altitude near the equator (due to the absorption of infrared radiation by aphelion water ice clouds) are not simulated, and modeled air temperatures aloft are too cold in comparison. It has been shown by Madeleine et al. (2012) that RAC is the basic solution to this issue.

In this modeling, dust was used as a "tuning knob" to help agreement with temperature observations aloft near the equator. For this purpose, dust is not a very effective "tuning knob", although a minimal enhancement of dust provides a small improvement. Experiments with larger dust enhancements were unsuccessful due to the different ways that water ice and dust interact radiatively, and further dust enhancement would have a negative effect on the simulation of the aphelion cloud belt in

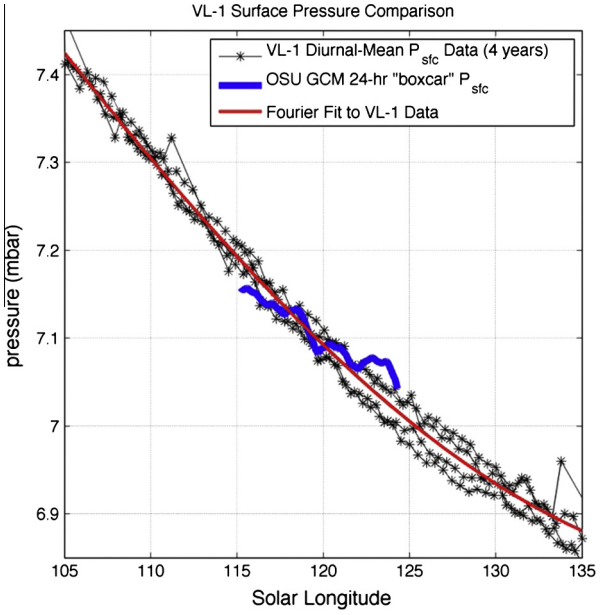

Fig. 2. The final 20 sols of surface pressure data from the NASA Ames GCM (interpolated to VL1 and adjusted for topography) are compared with VL1 observations. For VL1, the diurnal mean surface pressure data is shown. For the OSU MMM, a "boxcar" filter (with a 24 h window) is applied to the hourly GCM surface pressure record (blue curve). (For interpretation of the references to color in this figure legend, the reader is referred to the web version of this article.)

the OSU MMM (aphelion clouds are not the focus of this study). The opacity of dust (and its vertical structure) is tuned to provide a good agreement with TES observations in the northern polar region, the region where this study is focused. Poleward of ~45°N, both the Ames GCM and the OSU MMM agree very well with the TES observations. In Fig. 3, model zonal-means are constructed on the sigma levels of the two models. This provides a superior depiction of atmospheric structure near the surface. Near the pole, the near-surface OSU MMM structure is noticeably different from the Ames GCM. If the model zonal-means in Fig. 3 were constructed on a set of pressure levels (better for high in

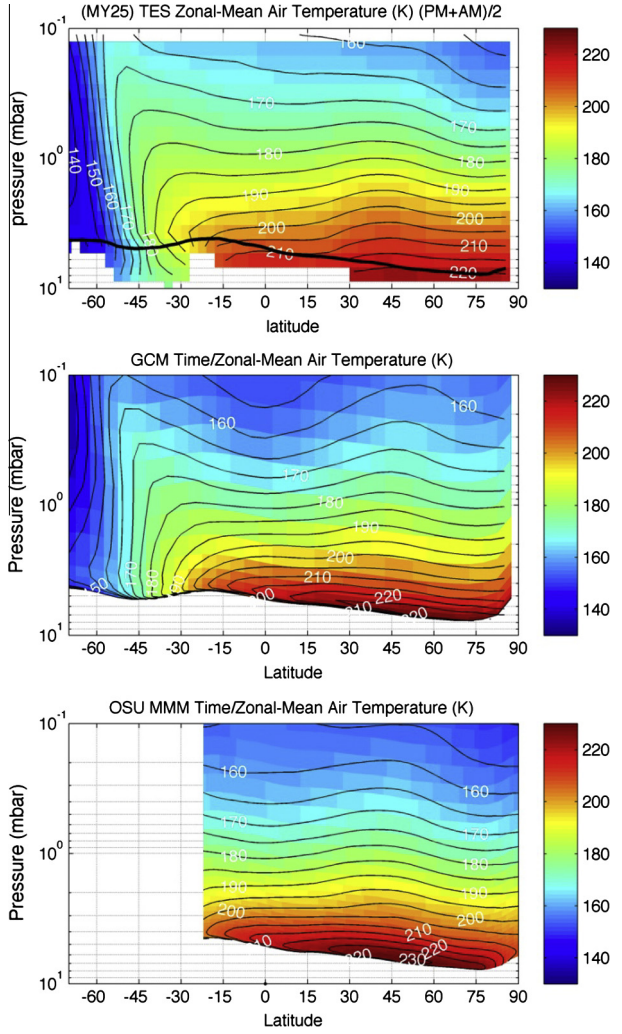

Fig. 3. TES atmospheric temperatures are compared with those from the Ames GCM and the OSU MMM for a period centered on $L_s = 120°$. TES temperatures are from MY 25, averaged over a $10°L_s$ window, where $T = (T_{PM} + T_{AM})/2$. The Ames GCM and OSU MMM temperatures are time/zonal-means for a period of 20 sols.

the atmosphere), the differences are small, similar to the differences between TES and MCS at $L_s \sim 120°$ when the atmosphere is consistently clear (David Kass, personal communication, 2013).

As in previous polar studies with the OSU MMM, the mother domain is polar stereographic and semi-global (see, for example, Fig. 2 in Tyler et al. (2008)). In this work the top of the model is at 1×10^{-4} mbar, with 55 layers in the vertical (60% are below 20 km AGL). In the center of the mother domain (at a nominal horizontal resolution of 135 km), two levels of two-way nesting are used: 45 km and 15 km. With two-way nesting, meteorological variables at co-located gridpoints in the lower resolution domains are set equal to the values of those variables in the higher resolution domains (and then a smoother is applied). The use of two-way nesting has important implications for later analysis, and the high-latitude differences in air temperature seen in Fig. 3 between the GCM and the OSU MMM are a consequence of two-way nesting and this feedback.

By examining the surface fields in the region that is key to this study (the polar region), the likely importance of two-way nesting can be seen. In Fig. 4, the topography and albedo fields of all three domains are compared for the polar region. The mother domain can be seen as a GCM analogue with no "pole problem", with somewhat better resolution than GCMs typically do when used for annual water cycle studies. The 45 km nest provides good resolution of the region, and the 15 km nest provides very good resolution, with the larger "spiral trough" features beginning to show on the polar dome. The OSU MMM is run for a total of 30 sols, seasonally identical to the second half of the GCM runs described above. The 45 km nest initializes four sols after the simulation begins, and the 15 km nest initializes four sols later. This timing gives two additional sols of spin-up at high-resolution (15 km) before the final 20 sols (that are centered on $L_s = 120°$). The final 20 sols of model output are used in the analyses for this study.

To initialize atmospheric temperature and winds in the OSU MMM, the use of interpolated GCM output (onto OSU MMM locations) is generally sufficient. In the atmosphere of a mesoscale model these fields fully spin-up to equilibrate with the higher resolution topography, the radiative forcing, and any differences in model dynamics and physics in ~2–3 sols. It is important to note that transient eddies play an important role in the high latitude summertime circulation. These eddies are resolved if the 45 km nest is active, and are resolved even better when the 15 km nest is active. They are not resolved in the GCM initial condition, nor if only the mother domain is active in the OSU MMM. Transient eddies constitute a larger-scale synoptic structure, and this means more spin-up time is required to fully establish the complex polar summertime circulation than for just the pseudo-cyclic mean diurnal cycles of temperature and winds (our experience shows that initializing nests as described above works well, Tyler and Barnes, 2005; Tyler et al., 2008). We have also found that ~20 sols is a sufficient period over which to perform an analysis of transient eddies in model results. The initialization of water vapor and cloud ice is described in Section 3.3.

2.2. The cloud scheme

Recently the OSU MMM has been modified to include the formation and evaporation of water ice clouds, the atmospheric sedimentation and fallout of ice particles onto the surface, the direct deposition of vapor onto the surface as frost and the re-sublimation of ice on the ground back into the atmosphere. The cloud scheme of Montmessin et al. (2004) was adopted as a template for the partitioning of atmospheric water between vapor and cloud ice. The scheme predicts the mean radius of ice particles based upon atmospheric conditions and a prescribed distribution for the number density and radius of dust particles that are allowed to be ice nuclei. The number of dust particles that can become ice nuclei is a prescribed fraction of the total number density, which is consistent with the dust distribution used for atmospheric radiation. Control of this provides a simple way to explore the importance of an explicit nucleation phase as a barrier to the growth of ice in the atmosphere. Our approach is similar to that of Madeleine et al. (2012), where a parameter is used to describe the ratio of the total number of dust particles to the number of condensation nuclei. As a baseline value in this study, 50% of the dust particles in an air parcel are allowed to serve as ice nuclei. In Section 3.4, four other cases are investigated in a parameter sensitivity and tuning exercise.

We modified the Montmessin et al. (2004) water mass conservation criterion so that the total water mass mixing ratio, the sum of the vapor (Q_v) and ice (Q_c) mass mixing ratios of an air parcel (not simply the sum of the mass density values), is conserved. This true mass conservation introduces an additional small term in the exchange equations that are now written in Q_v and Q_c. In a mesoscale model, where air temperature and density can change more rapidly due to the existence of strong smaller-scale circulations (sharper gradients in heating/cooling are expected), attention to mass conservation is important. However, little change is seen when using this modified criterion.

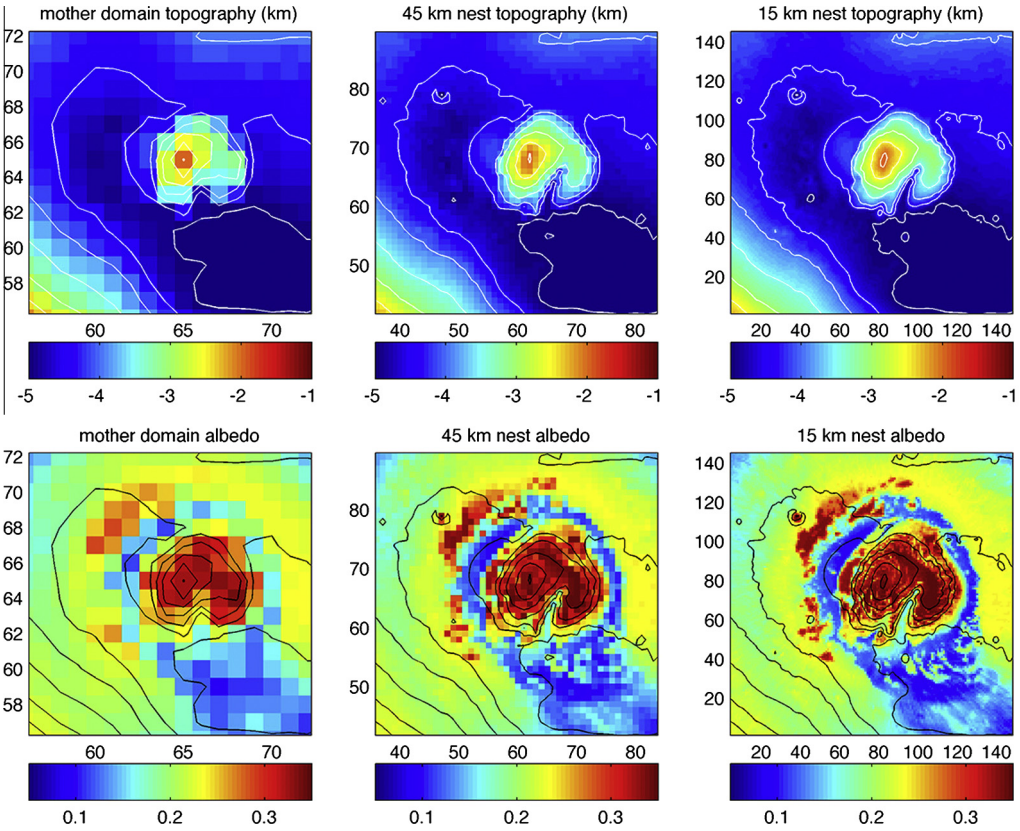

Fig. 4. The topography and albedo maps of all domains are shown as configured for this study (zoomed in on the identical polar region for each domain). The *X* and *Y* axes are labeled with domain gridpoint number for the subset of the domain being shown (the mother domain is 130 × 130 gridpoints with a nominal resolution of 135 km (true at 37.5°N), the first nest is 115 × 115 gridpoints at 45 km, and the second nest is 151 × 151 gridpoints at 15 km).

To address the fact that microphysical processes are faster than dynamical processes, the partitioning of water between vapor and ice is performed using two sub-timesteps for each dynamics timestep (dynamical timesteps are 45 s for the mother domain and three times smaller with each nest level). Offline experiments with a 1-D version of the cloud scheme show that using sub-timesteps for the vapor/ice partitioning in the microphysics yields more realistic water/ice phase transitions (eliminating oscillations due to overshoot/undershoot). Additionally, for the vapor and water ice fields, an "upwind" transport scheme has been adopted for advection. The original transport scheme produced "holes" in the vapor field (where the values of Q_v would sometimes become negative). Since "holes" must be "filled", water mass was not conserved. When using sub-timesteps, "noise" in the vapor/ice fields is visibly reduced, and with the upwind transport scheme "holes" are no longer produced, which causes water mass to be conserved to a very good precision.

Since an "upwind" transport scheme is diffusive in nature, some discussion regarding its adoption is needed. Before this code change, the Q_v and Q_c tendencies were modified by calls to three different subroutines that performed horizontal advection, vertical advection and diffusion. The horizontal advection scheme has been replaced with code that makes it an "upwind" scheme. In the present scheme, horizontal and vertical advection are performed in a single routine, where: (1) two sub-timesteps are used and (2) the total advection tendency is a consequence of considering the vertical and horizontal components simultaneously (arguably an improvement). This approach does not increase the computational expense, since there is no need to perform a diffusion calculation on the Q_v and Q_c fields. However, a diffusion calculation is performed for the highest resolution nest, since doing so causes the ice column to "look" more realistic in comparison with imagery over the NPRC. Because two-way nesting is used, regions where some diffusion might be desirable in the lower resolution domains are smoothed in the feedback process. The new advection scheme for the Q_v and Q_c fields was tested with sharp-boundary initial state cases (not shown), and it performs very well. A benefit of this approach is that the strength of diffusion for the winds is now separate from that for the Q_v and Q_c fields.

Finally, since cloud ice particles can fall to the ground (fallout), and frost can form on the ground due to the direct freezing of water vapor (deposition), a surface ice reservoir is needed to keep track of ice mass on the ground at off-cap locations in all modeling domains. The ice in this surface reservoir is free to sublimate back into atmospheric vapor when conditions allow (typically just after sunrise). Based on the examination of model results, where only very thin surface ice layers form (typically less than ~5 μm), the model surface albedo is not modified when ice is on the ground. As a result, ice that accumulates during the night probably sublimates too rapidly at sunrise. In future studies that will examine different seasonal dates, the surface albedo will be treated as a function of the mass of water ice on the ground.

In the model, deposition is treated with the same mathematical formulation as sublimation. The flux of vapor at the surface is equal to the product of a mixing coefficient, and the difference between the equilibrium vapor mass mixing ratio over ice at ground temperature, and the vapor mass mixing ratio of the lowest atmospheric layer ($Q_{eq} - Q_{air}$). The algebraic sign of the difference determines the direction for the possible flux of water vapor. The mixing coefficient is a function of air density, surface wind stress, moisture availability (*MAVAIL*) and a stability function as determined in the MRF PBL scheme as used in the OSU MMM (Hong and Pan, 1996).

For the sublimation of NPRC ices, *MAVAIL* = 1, while *MAVAIL* = 0.5 for the sublimation of off-cap snow/frost. For deposition (after some experimentation) we use *MAVAIL* = 0.1. During the simulation, mathematical checks assure that for deposition, and sublimation at off-cap locations, the vapor flux is not greater than the mass of water available would allow.

3. Tuning to the $L_s \sim 120^\circ$ season

For this study, a realistic representation of the observed $L_s \sim 120^\circ$ season is very important. The OSU MMM has been tuned to accomplish this, and the model improvements described above play an important role. In this section, tuning that is specific to this season is described, and the results are compared with observations. Specifically we address ground temperatures in the polar region, the initialization of atmospheric water (vapor and ice), and the values of unknown cloud scheme parameters that have an important effect on the amount of ice in the atmosphere.

3.1. High-resolution surface fields and ground temperatures

At the resolution of this modeling (~15 km), it is important to realistically simulate the sharp gradients in ground temperature that exist throughout the NPRC region. To achieve this, two problems must be solved: (1) accurate high-resolution maps of albedo and thermal inertia must be developed and (2) ground and soil temperatures must be initialized consistently with these maps and in the best possible agreement with available observations. With albedo and thermal inertia maps consistent with the mesoscale model resolution, a simple interpolation of GCM ground and soil temperatures leads to an unrealistic initial state. This is important, because the spin-up time for high thermal inertia locations is not short, especially so when initial temperatures are far from equilibrium. If due care is not given to this issue, the mesoscale model is unlikely to reach equilibrium before the end of a short (relative to the spin-up time required) simulation. In this study, dependent upon the spatial structure of the thermal inertia field, sharp contrasts in ground and soil temperatures are imposed on the initial state, as well as for each nest when it is initialized. The development of high-resolution albedo and thermal inertia maps is the first step.

The albedo and thermal inertia data of Putzig and Mellon (2007) guided the construction of the maps now used in the OSU MMM. The polar coverage of their maps is very good, although signal/noise issues at very high latitudes cause their data to be too "noisy" for direct use. Imagery does not have this specific problem. With some thought and effort, these two types of data can be combined to construct high-resolution albedo and thermal inertia maps, maps that have realistic values and the resolution needed.

Imagery provides the fine-scale spatial structure and the sharp gradients between surface types, whereas the Putzig and Mellon (2007) data guide the assignment of realistic values and control the more subtle regional gradients. In practice, a composite MARCI image that is centered in season on $L_s = 120^\circ$ is used (Wendy Calvin, personal communication, 2009). For high latitudes, at a resolution of 1/8 degree, the final albedo and thermal inertia data are shown in Fig. 5. An iterative process was used to refine these maps, as well as to "tune" the fixed temperature at the bottom of the soil model so that a seasonally appropriate surface heat flux (and therefore ground temperature) is simulated. Using the 20 sols of model output centered on $L_s = 120^\circ$, mean ground temperatures from the 15 km nest are determined (for TES AM and PM times) and then compared with TES in Fig. 6. In general, model temperatures differ by ~5 K or less, although at some locations (primarily near sharp gradients in albedo) the differences can reach ~10 K. Map refinement was performed under the guiding principle that bright locations (albedo) must also have somewhat greater thermal inertias. After several incremental changes, it was clear that further effort would be unproductive. For some very specific locations the guiding principle was proving unreliable. Further tuning would require the consideration of the vertical structure of the soil (with variable ice content) at very high resolution, a very difficult proposition in an environment that is also very dynamic. However, in closely matching TES ground temperatures, we have mapped out the surface locations (1) where ice can sublimate into vapor and (2) where sharp gradients in ground temperature will affect model dynamics. We experimented with maps where the moisture availability was determined by the thermal inertia of the location; in the end it was decided that a location simply can or cannot sublimate ice into the model atmosphere. In this study, if the thermal inertia of the location is greater than 600 units SI, the location can sublimate ice. For the 15 km nest (with this criteria), the total

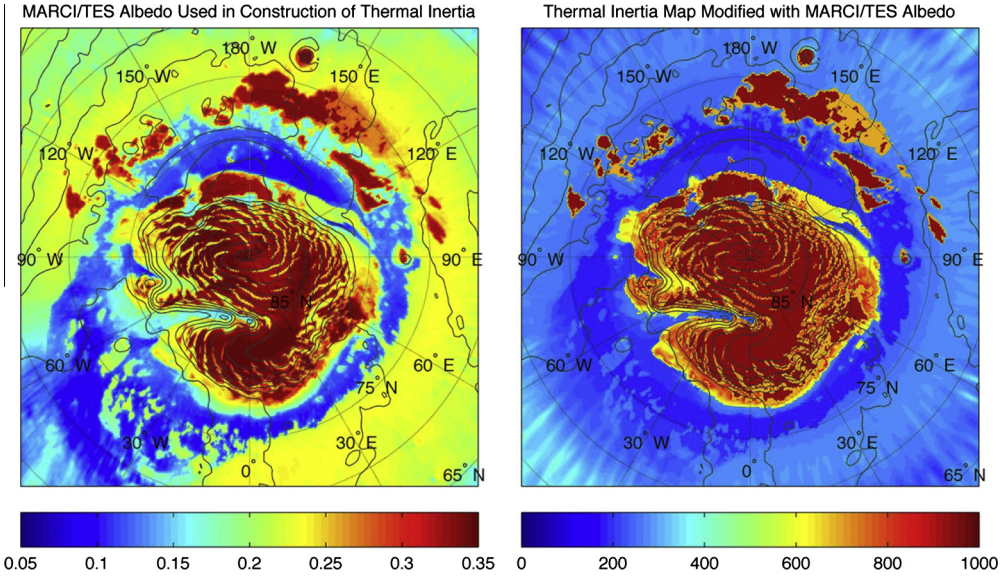

Fig. 5. Maps of surface albedo and thermal inertia (at eighth degree resolution) are shown. These maps are the basis of the maps used in all domains of the OSU MMM. The constructed data blends into the data of Putzig and Mellon (2007) between 60° and 70°N (the transition zone is apparent in the thermal inertia map).

area of exposed ice surface that can sublimate water vapor into the atmosphere is 1.20×10^6 km^2.

3.2. Comparison with Phoenix surface observations

Data from the Phoenix mission is an extremely valuable resource, and useful in the context of this work. Tamppari et al. (2010) provide a very good description of these data in a study using coordinated observations from Mars Reconnaissance Orbiter (MRO). Because of the relationship between air temperature and saturation vapor pressure, it is crucial that modeled air temperatures are in good agreement with observations. This is key for understanding differences between low-level clouds and ground fog predicted by the model and those observed by Phoenix, and is similar to wanting realistic ground temperatures for simulating sublimation rates and vapor column depths over the NPRC region. In Fig. 7, the Phoenix air temperature and surface pressure data are compared with OSU MMM results.

Air temperature results from the Phoenix location in the 15 km nest are compared with Phoenix data (at 1.9 m AGL) in the upper subplot of Fig. 7. The agreement is quite good, although the interpolated air temperatures (green circles) can be ~3–5 K too warm (primarily at night and early morning). Many factors may explain this, from the basic problem of vertical interpolation on a relatively coarse vertical grid to more physical issues regarding the performance of the PBL scheme in the very stable nocturnal surface layer on Mars. Certainly, small differences in the model albedo and thermal inertia values (constant over ~15^2 km^2 in the model), from the true smaller-scale local values, may be the main reason. When modeled ground temperatures are compared with observations from TES, the diurnal amplitude in the Phoenix region is in very good agreement with TES for this season (not shown), which suggests that model thermal inertia values are realistic for the region. Considering the good agreement in Fig. 3 at high-latitude with TES temperatures, the model is in very good agreement with the seasonal thermal environment.

The lower subplots of Fig. 7 show the 20-sol records of normalized surface pressure and excursions from the trended mean diurnal cycle for both the Phoenix lander and the OSU MMM. A "boxcar" smoother was applied to each record to aid the comparison. In the middle subplot of Fig. 7, the diurnal amplitudes are in good agreement, although the phases of the dominant diurnal modes are seen to differ by ~6 h. In earlier studies, comparisons with landed surface pressure observations were very favorable (Tyler et al., 2002; Tyler and Barnes, 2013). This either suggests problems with our modeling of surface pressure at high latitudes or with the data itself. For high latitudes at L_s = 120°, the real-world distribution of dust does not readily reduce to a simple function of latitude as well as it might for much lower latitudes. When maps of the three Mars years of TES infrared dust opacity are examined for L_s = 120°, this is readily seen. These maps show a similar high latitude structure that develops in all three years. This structure is

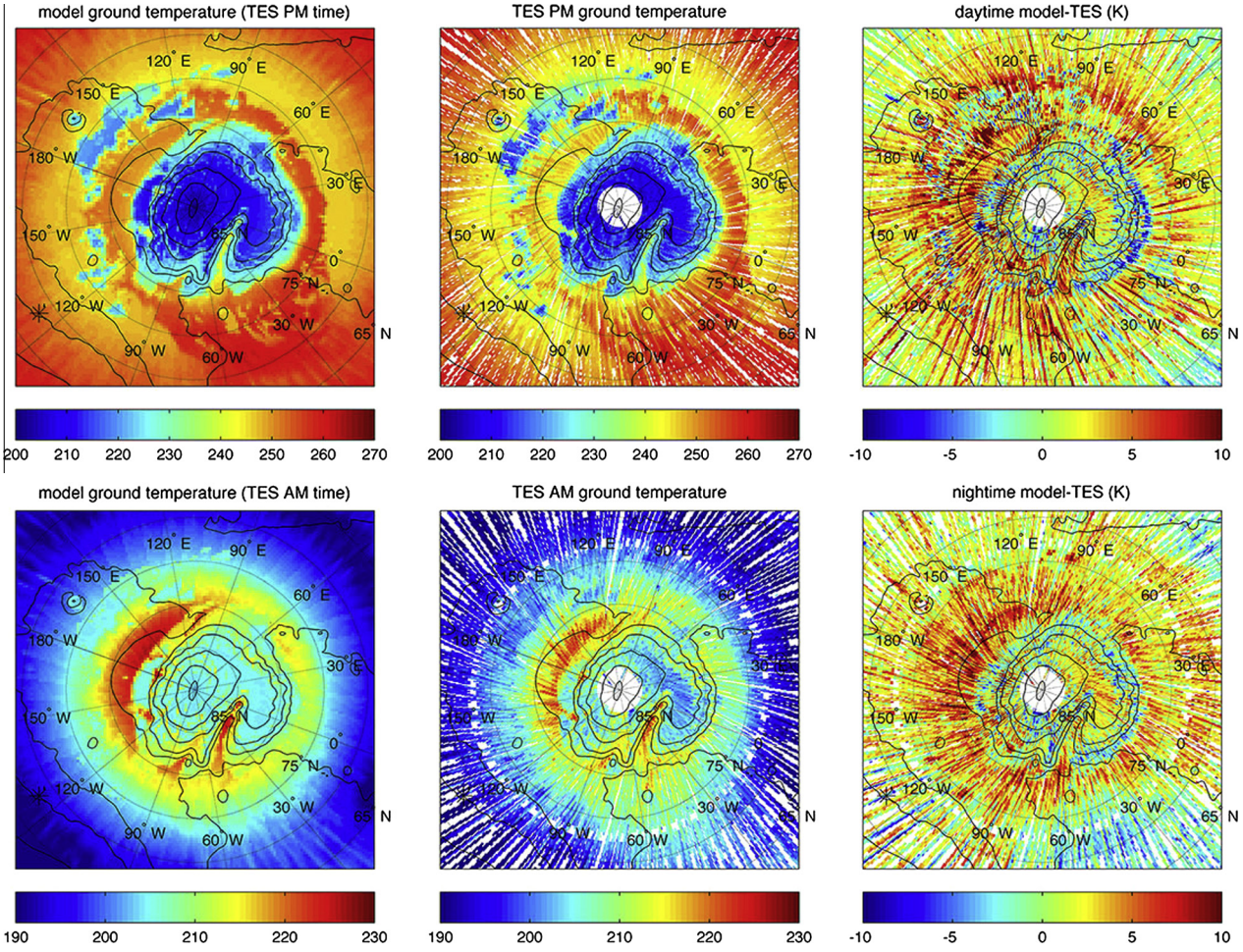

Fig. 6. A comparison between OSU MMM ground temperatures and TES data for L_s = 120° is shown. TES data were binned in half-degree spatial bins for a period of 5° of L_s to either side of L_s = 120°. The 20 sols of model data centered on L_s = 120° (taken from the 15 km nest) are used to construct the mean temperatures at TES AM and PM times (LTST varies significantly from 2 PM and 2 AM at high latitudes). The OSU MMM data are first interpolated to the TES bin locations before differencing.

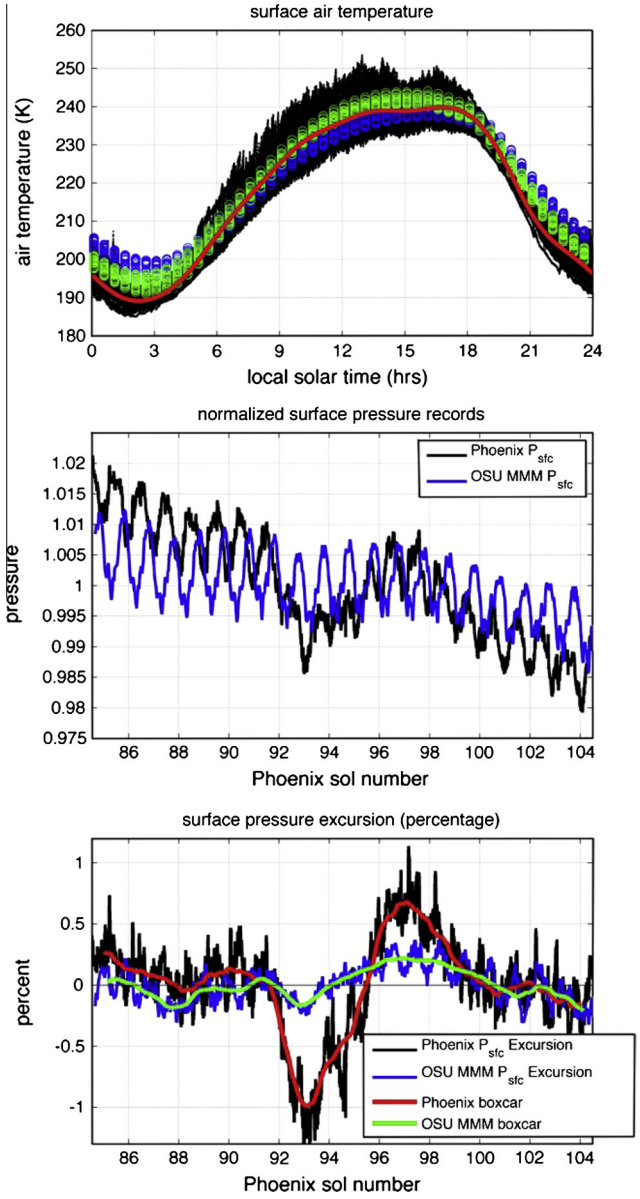

Fig. 7. A comparison between Phoenix air temperature and surface pressure data is made with the OSU MMM for 20 sols of data centered on $L_s = 120°$. In the upper subplot, records of air temperature are compared at 1.9 m AGL (the upper sensor on the Phoenix mast). The Phoenix data are shown in black with the 20-sol mean in red. The actual OSU MMM air temperature data (using the lowest model level at a diurnal mean height of ~7 m AGL) is shown with blue circles (the green circles show the result of vertically interpolating this data to 1.9 m AGL). The 20 sols of surface pressure data are compared in the middle subplot. In the lower subplot, excursions from the linearly trended mean diurnal cycles are shown. A "boxcar" smoother has been applied to facilitate an easier comparison between Phoenix (black/red) and the OSU MMM (blue/green). (For interpretation of the references to color in this figure legend, the reader is referred to the web version of this article.)

likely a consequence of larger-scale circulations, since the relatively sharp zonal gradients seen in the total column opacity do not correspond with topography. Tharsis is certain to play a role in forcing strong circulations into high-latitudes, as has been seen in past modeling efforts (Tyler and Barnes, 2005). The Phoenix region is likely under the influence of such circulations. It is possible that the zonal-mean dust prescription being used here does not cause a realistic radiative forcing of the atmosphere, even when the dust prescription is tuned to give good agreement with zonal-mean air temperature observations (Fig. 3). This could cause an unrealistic simulation of atmospheric tides and the surface pressure cycle to be in error. Possibly, 2-D dust maps are required in this context; Nelli et al. (2010) used 2-D maps in their Phoenix study, finding somewhat better agreement with Phoenix surface pressure observations than in this work (albeit for an earlier season). Finally, though, it is important to point out that the observed diurnal cycle of surface pressure may be subject to errors associated with temperature variations (Taylor et al., 2010; Peter Taylor, personal communication, 2013). Nevertheless, the primary reason for the surface pressure comparison in Fig. 7 is the dramatic and singular excursion centered on Phoenix sol number 94 ($L_s = 120°$). Possible problems with the diurnal cycle cannot affect this event recorded in the pressure record.

The large depression in the Phoenix surface pressure record reaches ~1% in the lower subplot of Fig. 7. This is the signature of a strong cyclonic transient eddy passing very near Phoenix, a singular event during this short period, although this remains the conclusion when an even wider seasonal period is examined. Shortly after this occurred (on sol 97), the Phoenix LIDAR observed a threefold decrease in the column dust opacity, and then a dramatic decrease in the height above ground where water ice clouds were seen (Whiteway et al., 2009). That these changes are dynamically related to the passage of a strong transient disturbance seems likely. The OSU MMM (or any mesoscale model) cannot be expected to simulate a specific transient event without the benefit of realistic synoptic initializations and short numerical weather prediction runs. However, the OSU MMM pressure record does exhibit a similar periodicity and amplitude for the passage of the smaller highs and lows seen in Fig. 7. Possibly, an important seasonal event has been captured in the Phoenix surface pressure data, and in this context the OSU MMM appears to perform realistically. In the model a strong cyclone (~1% surface pressure depression) passes to the east of Phoenix as it moves poleward. The seasonal context of this event is the recurring annular cloud first described by Cantor et al. (2002). An annular cloud is simulated with the OSU MMM in this study, and this is discussed below in Section 4.4.

3.3. Initializing water vapor and ice in the model atmosphere

Atmospheric water vapor and ice (clouds) are initialized in the OSU MMM using $L_s \sim 120°$ results from a multiple year run of the NASA Ames GCM. Mean diurnal cycles are formed, and these conditions are applied at the lateral boundary of the OSU MMM mother domain. For the mother domain interior, the initial vapor field from the GCM is modified to improve agreement with TES. A simple scaling factor (that varies only in latitude) multiplies the mass mixing ratios of water vapor to facilitate this. Since clouds in the GCM are too thick over the polar region, initial mass mixing ratios of ice are decreased appropriately. The lateral boundary of the mother domain is in the high tropics to midlatitudes of the southern hemisphere, where the GCM is in good agreement with TES, so the mean diurnal cycles of vapor and ice are unmodified. With this approach to boundary and initial conditions, initial agreement with the TES zonal-mean water vapor column is very good. Moreover, since both the sublimation of water ice and the transport of vapor in the model are realistic, the very good agreement holds for the 30-sol simulation. Using 10 sols of mother domain output centered on $L_s = 120°$, the 2 PM zonal-mean water vapor column depth is compared in Fig. 8 with TES for both MY25 and MY26. At all latitudes, the model agrees very well with MY25. Two curves are shown for each MY, one for the 5° of L_s period just prior to $L_s = 120°$ and one for the period just after. The multiple TES curves show that the zonal-mean vapor distribution is basically unchanging across the $L_s \sim 120°$ season, as simulated in the model.

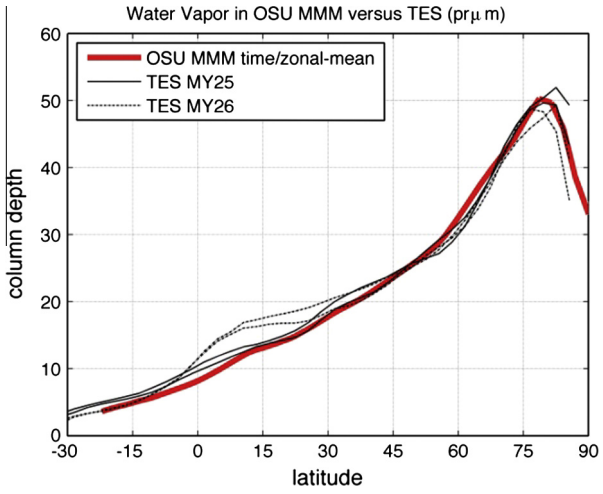

Fig. 8. The 2PM zonal-mean water vapor column abundance in the OSU MMM is compared with TES observations for MY25 and MY26. The model vapor data is from the mother domain of case 3 (~135 km spatial resolution), at a point in the run where both the 45 km and 15 km nests are active and fully spun-up (a 10-sol period centered on $L_s = 120°$). The TES data for MY25 and MY26 are 5° of L_s zonal-mean averages for two periods, one just before and one just after $L_s = 120°$, showing that there is no sizeable seasonal trend in either MY.

In developing this approach, numerous boundary and initial water vapor distributions were explored. At first these were numerical constructs, not based on GCM results. Even with a good initial agreement with the TES zonal-mean vapor column, the zonal-mean in the model could change rapidly, which is unacceptable for a 30-sol simulation. Three factors can cause this to happen: (1) an unrealistic initial vapor distribution, (2) unrealistic lateral boundary conditions, or (3) NPRC ices sublimating too much or too little vapor into the atmosphere. If these factors are not managed effectively, the model zonal-mean vapor column changes significantly and is still changing after a period ~10–20 sols. Dynamic adjustment of the vapor field cannot occur during a 10 sol spin-up period if the model is initialized too far away from equilibrium or with unrealistic boundary conditions. When studying seasonally specific aspects of the water cycle with a mesoscale model, it must simulate the observed larger-scale structure and trend, and validation of this is important. Therefore, the initialization of the model, as well as its dynamics and physics, is very important. Since only minimal trend is seen in the TES vapor column during the season centered on $L_s \sim 120°$, this is a very good season for an initial study where these modeling issues must be understood and managed. This will help when studying other seasons with sizeable trends that must be realistically simulated.

3.4. Cloud scheme parameter sensitivity

The recent laboratory work of Iraci et al. (2010) investigated the nucleation process for ice clouds on Mars. They found that nucleation is poorly understood, highly sensitive to temperature and requires greater levels of supersaturation than have been typically presumed. In the OSU MMM, the amount of cloud ice in the atmosphere is sensitive to two parameters in the cloud scheme: (1) the fraction of dust particles that are allowed to serve as ice nuclei (f_{IN}) and (2) a weighting factor that modifies the sedimentation flux of cloud ice (f_{SED}). These parameters are needed because the cloud scheme does not include an explicit nucleation phase, and only carries a single (mean) particle size from which sedimentation flux is determined. These two parameters serve as "tuning knobs", and provide a means to explore the poorly constrained physical processes involved in forming water ice clouds. In tuning to $L_s \sim 120°$ observations, we find that f_{IN} must be quite small in the northern polar region.

The number density of dust particles in the OSU MMM is prescribed to be consistent with the dust distribution used for atmospheric radiation. Nucleation is crudely represented when only a fraction of the dust particles are allowed to serve as ice nuclei. With f_{IN} equal to one, all dust particles are dust cores if there is ice in the air parcel. In this study, no more than 50% of the dust particles are allowed to be ice nuclei. Madeleine et al. (2012) used a version of the Montmessin et al. (2004) cloud scheme; and, to improve agreement with observations they limited the number of dust particles that can become ice nuclei to ~22%. A "semi-interactive" dust scheme was used in their study, so a direct comparison of f_{IN} values is not possible. In this study, four different meridional prescriptions for f_{IN} are explored: (1) a constant case with f_{IN} equal to 0.5, (2) a weakly limiting case where f_{IN} decreases from 0.5 to 0.05 between 55°N and 85°N, (3) a stronger limiting case where f_{IN} decreases from 0.5 to 0.025 between 45°N and 75°N, and (4) the strongest limiting case where f_{IN} decreases from 0.5 to 0.025 between 25°N and 55°N. The three prescriptions for f_{IN} that vary in latitude are shown in Fig. 9a. The small values chosen for the polar region (2.5% and 5%) bound the nucleation rate of a "few percent" that Daerden et al. (2010) found in their modeling of clouds and atmospheric ice as observed by LIDAR (Whiteway et al., 2009).

When the sedimentation flux of atmospheric ice is calculated in the model, a multiplicative factor (f_{SED}) is used to increase the radius of the single cloud particle size predicted. This only affects the calculated sedimentation velocity, and thus accounts for the role that more massive and faster falling particles would have if an actual particle size distribution had been simulated. Montmessin et al. (2004) explored a range of values (1.3–1.7) and suggested 1.5 provides the best fit for the water cycle, while Madeleine et al. (2012) adopted a value of 3. Here, two values are used, 1.25 and 1.75. Five simulations (from the eight possible combinations of parameter values) are used to explore the parameter space and facilitate model tuning. In all five cases both nests are active. The first case has f_{IN} constant at 0.5 with f_{SED} equal to 1.25 (case 1). The second case differs from the first in that f_{IN} varies according to the weakly limiting prescription (case 2). The third case uses the weakly limiting prescription with f_{SED} equal to 1.75 (case 3). The fourth case uses the stronger limiting prescription for f_{IN} with f_{SED} equal to 1.75 (case 4). The fifth case uses the strongest limiting prescription for f_{IN} with f_{SED} equal to 1.75 (case 5). The

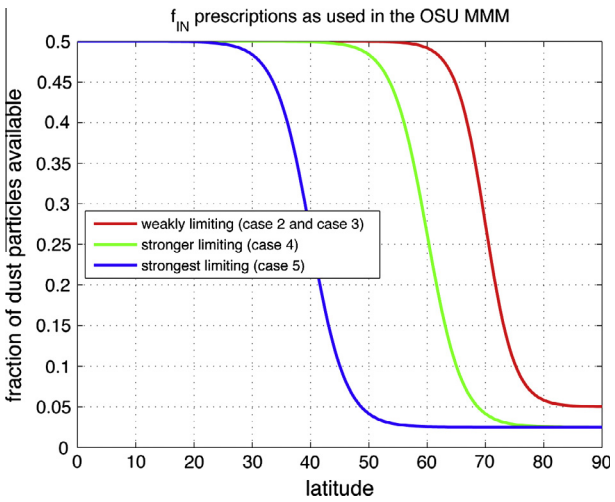

Fig. 9a. The three varying prescriptions, for the fraction of dust particles allowed to become ice nuclei (f_{IN}), are shown.

five cases are summarized below in Table 1. After processing ten days of mother domain output centered on $L_s = 120°$, zonal-mean column ice depths are constructed and shown in Fig. 9b (cases 1–3) and Fig. 9c (cases 3–5).

In all five cases, model results are compared with zonal-mean ice column depths that have been constructed from TES IR (12 μm) ice opacity data. A highly simplified relationship is used to convert the TES infrared opacity data to column ice depth: $d_{vapor} = 2 \times R_{cloud} \times TAU_{IR}$ (M. Smith, personal communication, 2008). In using this relationship, a cloud particle radius of 4 μm is presumed. This is representative of the aphelion cloud belt particles seen in this study. For the five cases that are shown in Figs. 9b and 9c, this relationship allows for a crude comparison with the observed meridional structure of atmospheric ice. Importantly, Figs. 9b and 9c provide direct comparison for the amount of ice in the atmosphere of each case, which avoids the uncertainty that particle size causes when opacity is the only metric used in comparison. For each of the five cases, two model profiles are compared with TES. The blue curves are time-mean and zonal-mean profiles (all times of day are utilized), and the red curves are 2 PM local solar time profiles (for comparison with TES).

In cases 1 and 2 of Fig. 9b, f_{IN} is 0.5 south of 55°N, where the results for both cases are the same. In case 2 at 85°N, where the value of f_{IN} has decreased to 0.05, the ice column depth is ~50% of that in case 1. With only 5% of the dust particles allowed to become ice nuclei, cloud particles grow larger. This increases fallout onto NPRC ices and into lower atmospheric layers where cloud particles are more likely to sublimate. Over the pole, the diurnal cycle in air temperature is small, and ice column depths are almost identical for both the diurnal mean (blue) and the 2 PM (red) profiles. In case 3, where the ice sedimentation flux is enhanced by the larger value ($f_{SED} = 1.75$), ice column depths are smaller at all latitudes. In midlatitudes the difference between the diurnal mean and the 2 PM profiles is notably more pronounced in case 3 than in case 2. A simple explanation seems likely: with greater sedimentation flux, there will be a larger diurnal cycle in the ice column simply due to the sublimation of ice particles in warmer layers lower in the atmosphere.

Cases 3, 4 and 5 are compared in Fig. 9c. In cases 4 and 5, greater limitation is put on f_{IN}. The minimum value of f_{IN} is smaller and the parameter remains small closer to the equator. For case 4, with the stronger f_{IN} prescription in use (see Fig. 9a), significant differences are seen poleward of ~50°N where the prescriptions for case 3 and case 4 diverge. In high midlatitudes, the ice column abundance in case 4 changes opposite to that of case 3, decreasing with latitude until the steep increase into the most polar latitudes begins. In case 4 the increase is more pronounced than in case 3, although it happens at basically the same latitude, just poleward of ~70°N. Examining the prescriptions for f_{IN} in Fig. 9a, the value is decreasing rapidly for case 3, whereas for case 4 it is approaching the 2.5% minimum. In Fig. 9c, the TES constructions do exhibit a small upturn poleward of ~75°N. While the value of f_{IN} certainly affects the amplitude of the upturn in the model column depths, it does not seem to have a controlling effect on the latitude where it grows steepest. This may be a basic consequence of the meridional structure of water vapor (that is almost exactly the same in all five cases), as well as possibly the strength of the diurnal cycle (which is far weaker when the Sun never sets). In case 4, with only 2.5% of the dust particles able to become ice nuclei at high latitudes, the ice column depth over the polar region is further reduced, to ~0.7 μm, a reduction of ~23% compared to case 3. The latitude of the minimum in case 4 might be seen as being in better agreement with the data. With case 5, the ice column depth exhibits an upturn towards the equator before the value of f_{IN} actually begins to increase towards the equator. Certainly, case 5 indicates that very small values of f_{IN} are unrealistic in the midlatitudes. Comparing these cases suggests that small values are required in polar latitudes. With regard to physical constraints, however, it is not at all clear how one would best prescribe meridional variation of f_{IN} .

Even with large differences in f_{IN} between the cases described above, a broadly similar meridional structure remains. In a very basic sense, there are two environments in which clouds form: (1) an environment with high vapor abundance and a relatively

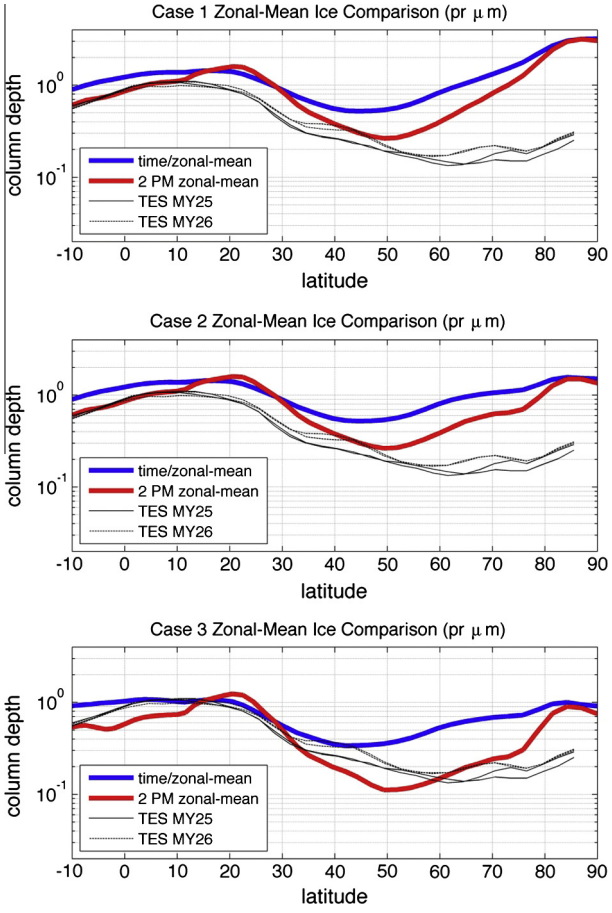

Fig. 9b. Results are shown for three of the parameter sensitivity simulations. Case 1: f_{IN} is everywhere equal to 0.5 with f_{SED} equal to 1.25. Case 2: f_{IN} decreases in high northern latitudes with the weakly limiting prescription (see Fig. 9a) with f_{SED} equal to 1.25. Case 3: f_{IN} decreases in high northern latitudes according to the weakly limiting prescription with f_{SED} equal to 1.75. The TES MY25 and MY26 data are zonal-mean ice column depths, constructed from the TES 12 μm IR opacity data using a relationship given in the text. Two profiles are shown for each MY, each an average over a 5° L_s bin period, with one just before and one just after $L_s = 120°$. The OSU MMM zonal-means are constructed using 10 sols of data centered on $L_s = 120°$. The blue curves are time/zonal-means, while the red curves use 2 PM local solar time model results (best for comparison with TES). (For interpretation of the references to color in this figure legend, the reader is referred to the web version of this article.)

Table 1
The values of f_{IN} and f_{SED} are shown for each of the five cases explored in the parameter sensitivity and tuning exercise described in this section. Case 3 (bold font) provides the best agreement with observations, and is used primarily in later analyses.

Case #	f_{IN}	f_{SED}
1	Constant: 0.5	1.25
2	Weakly limiting: 0.5 at ~55°N to 0.05 at ~85°N	1.25
3	**Weakly limiting: 0.5 at ~55°N to 0.05 at ~85°N**	**1.75**
4	Stronger limiting: 0.5 at ~45°N to 0.025 at ~75°N	1.75
5	Strongest limiting: 0.5 at ~25°N to 0.05 at ~55°N	1.75

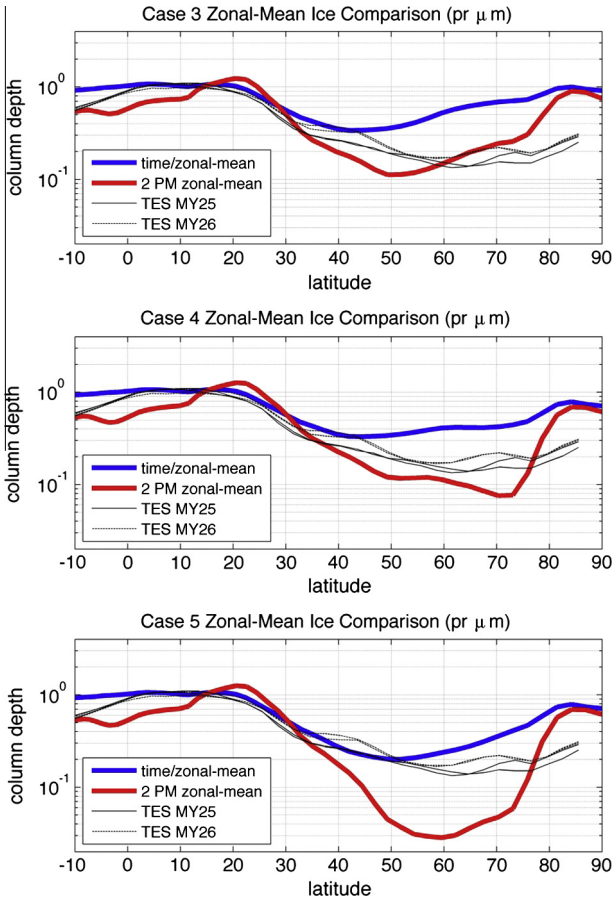

Fig. 9c. As in Fig. 9b, results for three of the parameter sensitivity simulations are shown. Case 3: f_{IN} decreases in high northern latitudes according to the weakly limiting prescription with f_{SED} equal to 1.75. Case 4: f_{IN} decreases to the north according to the stronger limiting prescription (see Fig. 9a) with f_{SED} equal to 1.75. Case 5: f_{IN} decreases to the north according to the strongest limiting prescription (see Fig. 9a) with f_{SED} equal to 1.75.

small diurnal cycle of temperature and (2) an environment with rather vigorous vertical motions and a much larger diurnal cycle of temperature. In the first class smaller supersaturations would be expected; larger supersaturations would be expected the second class. In the first class, after a small fraction of dust particles nucleate, the remaining fraction could be prohibited from nucleating due to their likely smaller size and the growth of those already nucleated (the dust particle size dependence for nucleation is very important). This would lead to small nucleation fractions (the larger dust particles primarily) and much larger cloud particles. In the second class, stronger dynamics and larger diurnal cycles would lead to greater supersaturations, which should cause far more dust particles to nucleate (over a wider range of dust particle sizes), resulting in a greater number of smaller ice particles. For $L_s \sim 120°$, the best agreement with observations occurs when large values of f_{IN} are used south of some high latitude. In fact, when a run was performed with f_{IN} everywhere at 5%, very large particles ($\sim$100 μm) were seen to form in the tropics that would fall to the ground over Tharsis at night. The amount of ice falling to the ground was so great that the local vapor column would grow as large as that over the polar region when it sublimated after sunrise, which is entirely unrealistic (results not shown). We conclude that the fraction of dust particles that nucleates must vary greatly in latitude for $L_s \sim 120°$, being quite small over very high latitudes and growing much larger towards the equator (possibly approaching unity). This conclusion gains support when nucleation rates are examined in a GCM with a more complete microphysics scheme (Thomas Navarro, personal communication, 2013).

3.5. Model visible opacity and particle size

An important way to check model results is to construct the opacity of ice in the model and make a direct comparison with TES opacity observations. Using vertical profiles of the dust number density (N_{dust}), the fraction of dust particles allowed to become ice nuclei (f_{IN}) and the radii of cloud particles (R_c) at a local time of 2 PM in the model, the column visible opacity of water ice is computed as follows:

$$\tau_{\mathrm{vis}}(\lambda,\phi,z) = \int_0^{\infty} f_{IN}(\phi) N_{\mathrm{dust}}(\lambda,\phi,z) Q_{\mathrm{eff}} (\pi R_c^2(\lambda,\phi,z))\, dz.$$

In this expression Q_{eff} is equal to 2, to a very good approximation regardless of particle size. Using ten days of results from cases 3 and 4 centered on $L_s = 120°$ (the same data period used for Figs. 9b and 9c), the time/zonal-mean result is compared in Fig. 10 with the TES visible opacity (assumed to be 2.1 times the TES 12 μm IR opacity). The red curve in Fig. 10 is case 3, in good agreement with TES. If we presume that the TES opacity is sensitive to cloud ice existing in the first scale height above the ground at high latitudes, f_{IN} values in the $\sim$5% range (near that suggested by Daerden et al., 2010) provide very good agreement with the data. For case 4 (blue curve), the value of f_{IN} remains small much further towards the equator (see Fig. 9a). The comparison shown in Fig. 10 further supports the assertion that, at some polar latitude just south of the NPRC, small nucleation fractions become unrealistic (certainly in a zonal-mean sense).

When the shape of the opacity profiles in Fig. 10 is compared with the column depth profiles in Fig. 9c, there are notable differences. For the aphelion clouds, there is little difference between Fig. 9c and Fig. 10, although the opacity agreement appears worse since Fig. 9c uses a log ordinate. Poleward of $\sim$30°N in Fig. 10, case 3 is in very good agreement with TES, even showing a relative maximum at $\sim$67°N. The key difference is seen in comparison to the ice column depth at high latitude, where the maxima in the case 3 opacity is $\sim$1/3 that in the aphelion cloud belt (a $\sim$66% decrease). For the ice column depth, the value over the pole is only $\sim$25% less than that in the aphelion cloud belt. The reason for this is simple: ice particles are much larger in the polar region because f_{IN} is small. With the depth of the ice column proportional to particle radius cubed and the opacity proportional to particle radius squared,

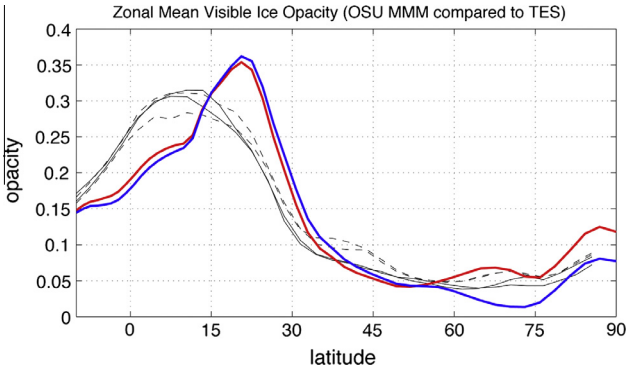

Fig. 10. The zonal-mean model visible ice opacity at 2 PM is compared to the TES visible ice opacity (2.1 times the IR opacity). The solid red curve is for case 3, and the blue curve is for case 4 (see Fig. 9c). For TES, MY25 is shown with solid black lines and MY26 is shown with dashed black lines. Two profiles are shown for each MY, each an average over a 5°L_s bin period, with one period just before and one just after $L_s = 120°$. (For interpretation of the references to color in this figure legend, the reader is referred to the web version of this article.)

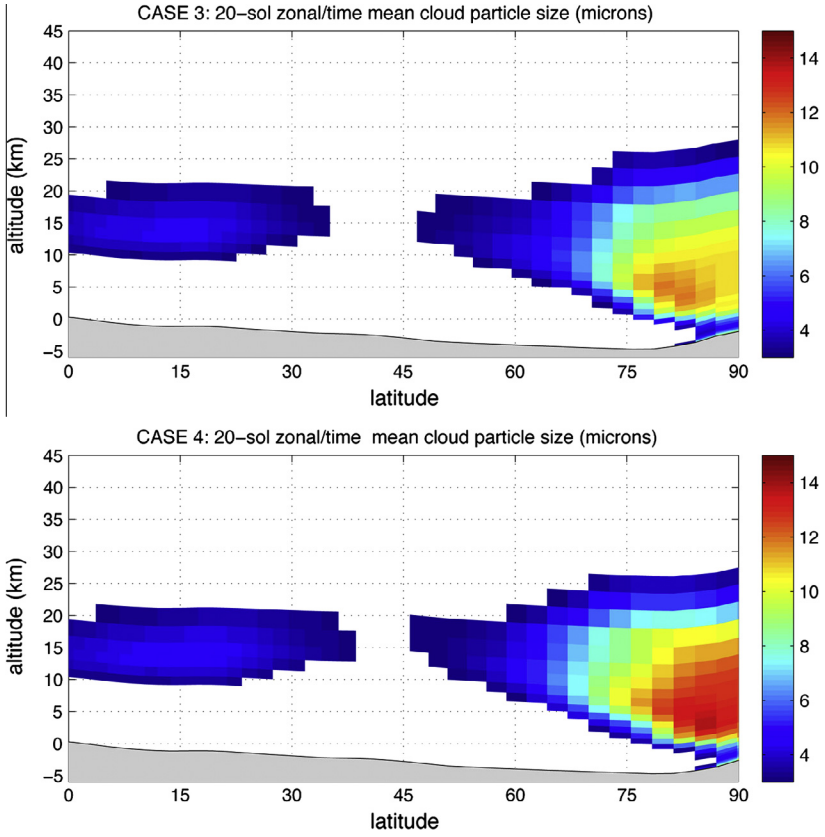

Fig. 11. The 20-sol time/zonal-mean ice particle sizes are shown for case 3 and case 4 (see Figs. 9a, 9c and 10).

significant differences will be seen if cloud particle size varies significantly with latitude. For cases 3 and 4, Fig. 11 helps to quantify this by showing the zonal-means of the diurnal mean cloud particle sizes (20 sols of data are used). There is a sizeable difference between ice particles in the aphelion cloud belt and those in the polar latitudes.

Opacity observations are an incomplete constraint. Visible imagery (MOC and MARCI) provides additional constraint on polar cloudiness over a wider local time range, although it is difficult to extract opacity or particle sizes from imagery. Since water ice clouds are central in ongoing studies of the martian climate, better constraint on the size of cloud particles is needed. It is noteworthy that excessive cloudiness is a modeling problem in the northern polar summertime, when there is the greatest amount of atmospheric vapor. This season and region are critically important for understanding water ice clouds. Because the dust and water cycles are so closely linked, future studies (to develop a more general approach) will require an explicit nucleation phase and careful consideration of how well it is performing.

4. Results

4.1. Polar cloudiness decreases with increasing spatial resolution

The NPRC region is highly complex, which likely causes the circulation to be so as well. A key aspect of this study has been to investigate the effect that model resolution has on the results, specifically the amount of cloud ice in the polar summertime atmosphere. As described by Haberle et al. (2011) and explored by Madeleine et al. (2012), GCMs have tended to simulate too much ice in the northern polar summertime. Exacerbating this problem, radiatively active water ice clouds (RAC) cool the lower atmosphere, which causes more clouds to form in a positive feedback loop with a great deal of sensitivity to poorly constrained parameters. Since insolation cannot reach the ground with thick RAC, the sublimation of water ice must decrease because of lower daytime ground temperatures, and this dries out the water cycle in comparison to observations. Given the complexity of the region, an examination of the circulation needs to be part of comprehensive efforts to understand this problem.

The basic effect that model resolution can have on the circulation can be seen with an additional simulation, one configured as for case 3 (described in Section 3.4), except the nests are never activated. Thus, spatial resolution in the polar region is that of the mother domain (nominally 135 km, ~160–165 km near the pole), instead of the resolution of the second nest (nominally 15 km, actually ~18 km). Without nests, the area of a model gridpoint is 81 times greater than in the high-resolution simulation (see Fig. 4). This additional simulation provides a GCM analogue for case 3.

In Fig. 12a, the spatial distribution of the diurnal mean ice sublimation is shown for both cases. The total sublimation rates and the total areas of ice available for sublimation (exposed ice) are given in the subplot titles of Fig. 12a. The total sublimation rate is ~25% greater in the high-resolution case, although this does come from a total ice area that is ~10% greater (a location can sublimate ice into atmospheric vapor if its thermal inertia is greater than 600 units SI). In the left subplots, local diurnal mean sublimation rates are shown (for a 20-sol mean at L_s = 120°). The right subplots identify all of the ice locations and show whether the net local effect is sublimation or deposition. At 15 km resolution, the largest local sublimation rates can be ~2 times greater, while the area weighted sublimation rate is larger by only ~25% (probably

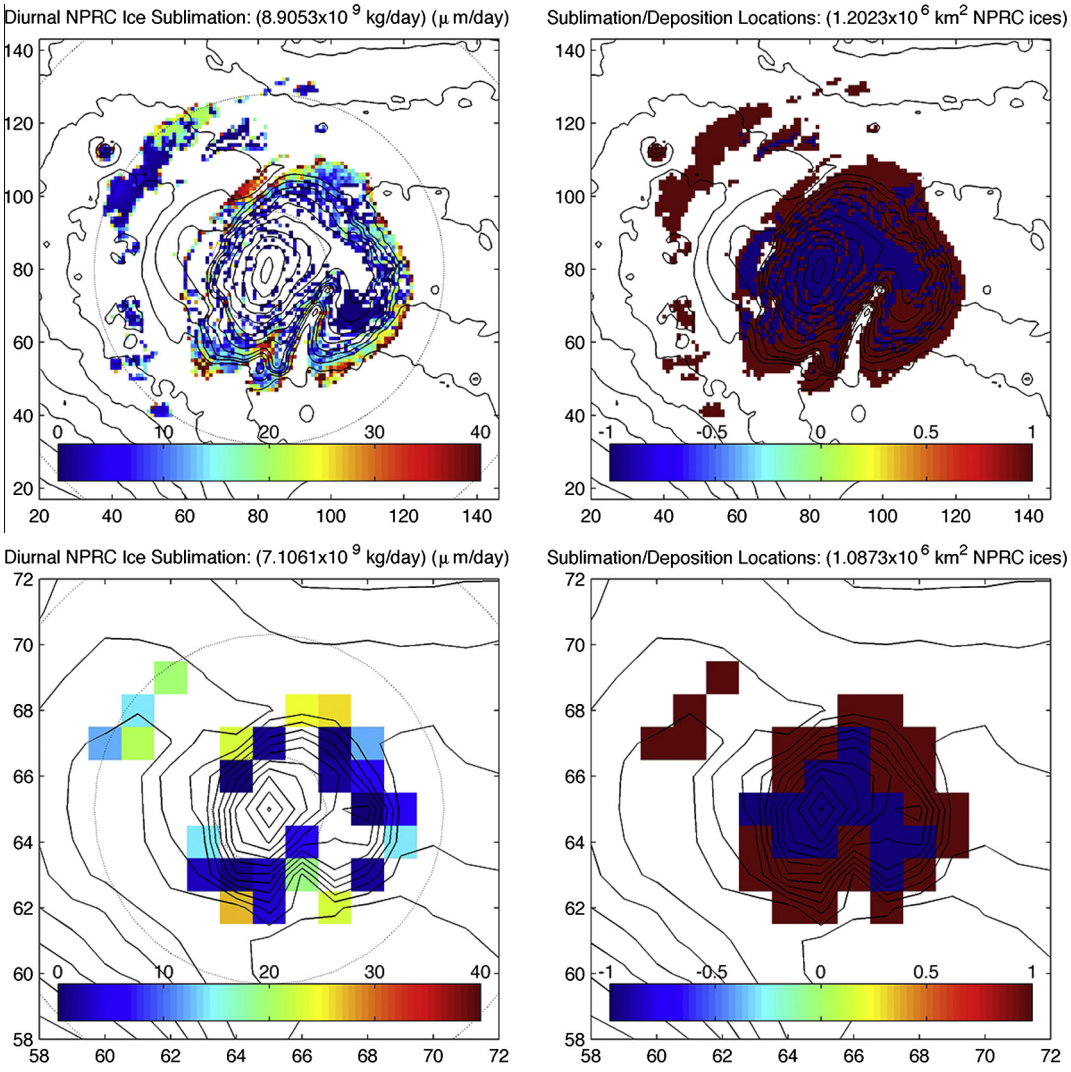

Fig. 12a. In the left subplots, the 20-sol diurnal mean sublimation rates are shown for the high-resolution case and the low-resolution case (spatial resolutions are nominally 15 km and 135 km, with case 3 parameters used in both simulations). Regions of net sublimation and net deposition are indicated in the right subplots at all permanent ice locations (thermal inertia greater than 600 units SI). The total area of permanent ice in each of the two cases is provided in the title. In the left subplots, local sublimation rates are shown in color (μm/day), and the total sublimation of ice mass per day is given in the subplot titles. The *X* and *Y* axes are labeled with gridpoint number for the subset of the specific domain shown.

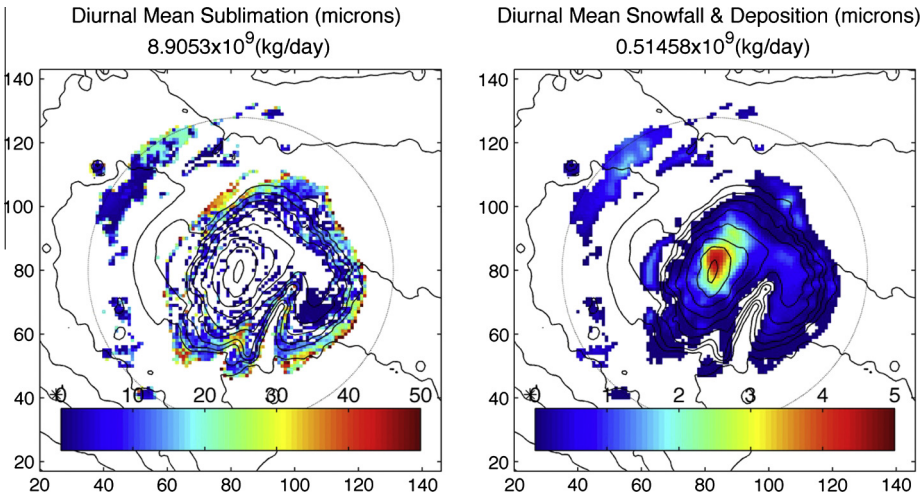

Fig. 12b. The loss (sublimation) and accumulation (deposition/snowfall) of ice is shown for the 15 km nest of case 3. In the left subplot the sublimation rate (as in Fig. 12a) is shown. In the right subplot the sum of the snowfall and deposition rates is shown.

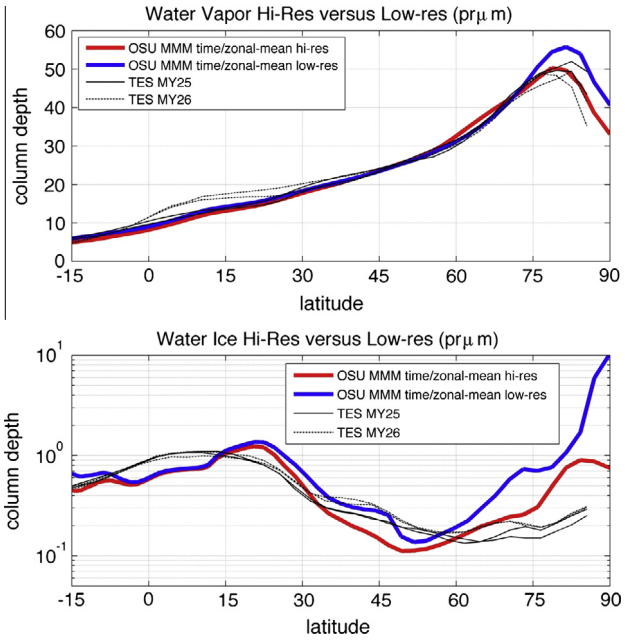

Fig. 13. Two simulations are compared, a low-resolution case (without nests) and a high-resolution case (with nests). The upper subplot shows the column water vapor depths compared to TES. The lower subplot shows the column ice depths compared to TES. The two curves for each TES MY show the 5°L_s bin period for just before and after L_s = 120°.

somewhat larger due to the ~10% greater ice area). Since resolution accurate maps of albedo and thermal inertia are used for every modeling domain, the total ice areas agree fairly well, especially with such a dramatic difference in spatial resolution between the two cases and so much complexity in the surface thermal properties (see Figs. 4 and 5). In this context, the results from these two cases are in reasonable agreement.

In Fig. 12b, sublimation (loss) is compared with the sum total of fallout and deposition (gain), which reveals there is a net accumulation of ice at the most polar latitudes. This depicts the NPRC ice budget at $L_s \sim 120°$ for the high-resolution case, and shows that the combined rate of fallout (snow) and direct deposition of vapor (frost) is only ~6% of the total sublimation rate. The accumulation of ice on the polar dome in summertime may indeed be climatologically significant, although it does not have an important role in this analysis (even if considered, there is still a larger flux of vapor into the atmosphere of the high-resolution case).

Turning to the atmosphere, in Fig. 13 we compare the 2 PM zonal-mean vapor and ice column depths from the mother domains of both cases (data are compared with TES as in Figs. 9b and 9c). Since two-way nesting is used, the mother domain is fully consistent with the higher resolution nests (the two-way nesting sets mother domain variables equal to those at co-located gridpoints in the higher resolution domains, and then a smoother is applied that functionally lowers the resolution). In the upper subplot of Fig. 13, the low-resolution case has ~5 pr μm more water vapor in the polar atmosphere. The lower subplot of Fig. 13 shows that the low-resolution case has ~10× more cloud ice in the atmosphere. A direct relationship between vapor and cloudiness is expected; however, in consideration of Fig. 12a, the results of Fig. 13 would not be expected unless the circulation (as resolved with resolution) plays an important role in the ventilation equatorward of the additional vapor sublimated into the high-resolution case.

Given the complexity of the polar region, a logical hypothesis is that vapor and ice amounts are smaller in the high-resolution case because important aspects of the circulation can only develop with sufficient resolution. Stronger circumpolar winds, highly specific locations for ice sublimation and strong transient circulations are all key aspects of the circulation at high-resolution. With sufficient resolution, ice sublimates rapidly at locations where it can be ventilated off the NPRC much more readily. Sufficient resolution (which causes realistic gradients in surface properties to exist) is the basic explanation for the strength and complexity of the circulation. Resolving this complexity, specifically the scales of action on which important dynamical forcing occurs, may be the only way to simulate a sufficiently realistic circulation and the resulting effect seen in the water vapor and water ice column depths.

The circulation in the high-resolution cases modifies the zonal-mean structure of air temperature and winds at very high latitudes in comparison to the case without nests. This is shown in Fig. 14a. Significant differences are seen in the lowest ~5 km of the air temperature fields. The decrease in air temperature with latitude is gradual in the case without nests, and there is even an increase with latitude right at the pole. In the case with nests, the temperature barely changes with latitude until the rapid decrease begins just poleward of ~75°N (this is also seen in Fig. 3, where the OSU MMM mother domain of case 3 is compared with the GCM). Strong transient eddy activity exists in these latitudes when nests are active (as described below), although it is not seen in the case without nests or in the GCM. There is insufficient resolution for the formation of transient eddies without at least one active nest. In the zonal and meridional wind comparisons of Fig. 14a, low-level easterlies and katabatic flow are not seen in the case without nests; the circulation is in fact unrealistic. The temperature and wind fields are closely related dynamically, and if the model is not capable of resolving the important scales of dynamical action, nor transient eddies, the circulation cannot be realistic.

Without nests, the scales of dynamical forcing in the polar region are ~$2\Delta x$ (see Fig. 4). At these scales, the 4th order horizontal diffusion used in the model is designed to remove sharp features in the circulation. To test whether this diffusion is possibly too strong (not allowing a more realistic circulation to form), another run was performed with its strength half the nominal model value. In comparison with Fig. 14a, only negligible changes in the zonal-mean fields were seen, while some other behavior seemed to suggest that the diffusion had been made too weak (not shown). Two more tests were performed: (1) the number of microphysics timesteps for each dynamical timestep was increased by 3× to compare directly with the situation when the first nest is active and (2) the polar topography was smoothed to remove the requirement that co-located gridpoints have the same value (needed for two-way nesting). Neither of these tests resulted in any real difference from the left subplots of Fig. 14a. Finally, Fig. 14b shows the vertical structures responsible for the column depths shown in Fig. 13, the zonal-means of the mass mixing ratios of water vapor and cloud ice (Q_v and Q_c) for the two cases. An unrealistic circulation leads to the accumulation of water vapor and ice over the NPRC, whereas a realistic circulation is effective at ventilating vapor equatorward.

All atmospheric models are tuned to perform better in comparison to observations. Tuning can compensate for poorly constrained or insufficiently realistic implementation of physical processes, and may even serve to improve results when important dynamics are not resolved. Without an extensive set of observations (as with terrestrial studies), determining what causes a "tuned" model to get the right answer becomes increasingly challenging as the number of parameterizations grows. In a "typical" gridpoint GCM for Mars (with a spatial resolution of a few degrees), the circulation in the northern polar region during summertime is not sufficiently resolved. This study strongly suggests that a minimal resolution of the key aspects of this circulation is necessary to

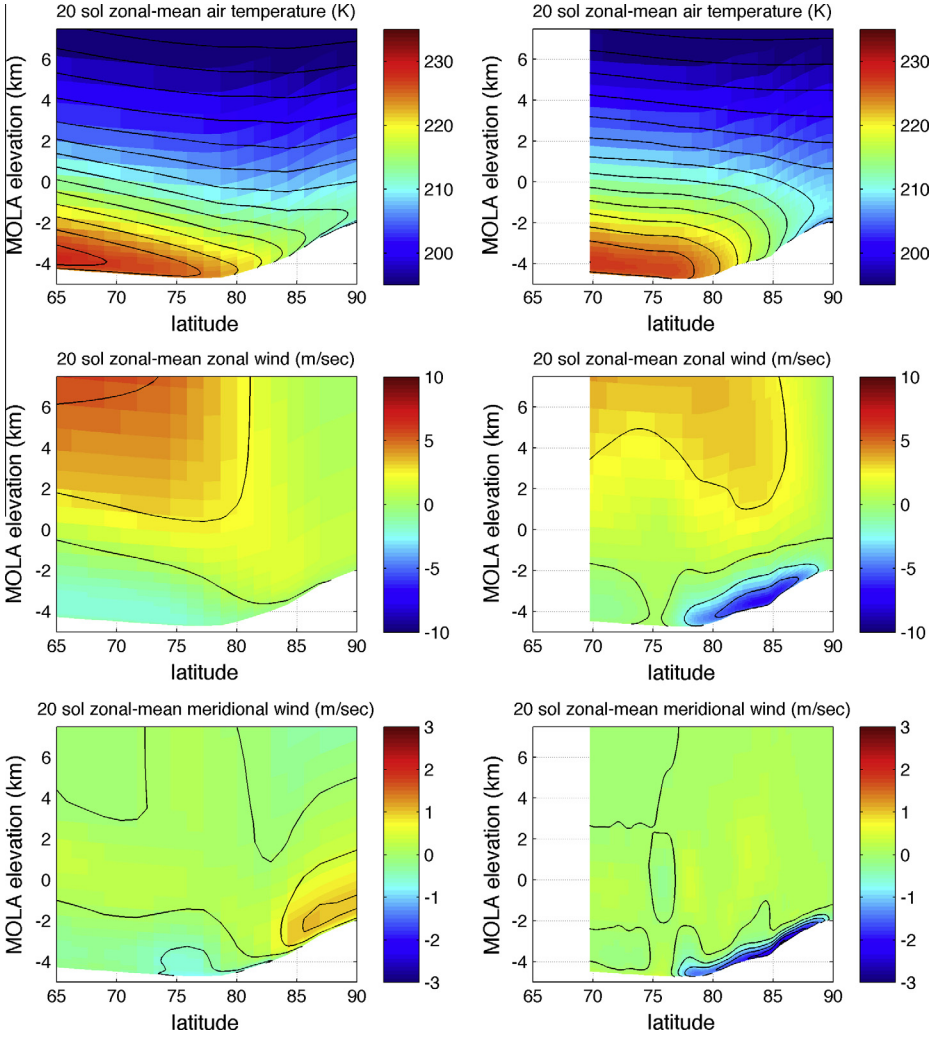

Fig. 14a. 20-sol time/zonal-means are shown for air temperature, zonal wind and meridional wind. The left set of subplots is from a case without nests (mother domain only, a resolution of ~135 km). The right set of subplots is from the 15 km nest in the case with both nests active. Both simulations use case 3 cloud scheme parameters.

obtain a realistic simulation of water ice clouds. There are a couple ways that GCMSs could explore this. A cube-sphere grid GCM was used by Lian et al. (2012) to simulate the seasonal enhancement of argon gas in the polar atmosphere of Mars, and in the absence of the "pole problem" they saw improved results. Since the OSU MMM does not have a "pole problem", sufficient resolution appears to remain important in this specific context. A GCM with a spectral dynamical core may have advantages, since the filtering that is required for maintaining numerical stability in a gridpoint model is not required (this filtering functionally turns the GCM into a 2-D model near the poles).

In the runs described here, the first nest (at 45 km) initializes after four sols and the second (at 15 km) after another four. In a two-nest simulation, the very large ice column amounts over the polar region disappear within a single sol after the first nest is initialized. Initialization of the second nest four sols later does not produce another decrease in column ice depths over the polar region, which seems to suggest that a spatial resolution of ~1° could provide a sufficiently realistic polar circulation (especially on a cube sphere grid). This hypothesis was tested with an additional full-length simulation where only the 45 km nest is activated, and any differences with the right subplots of Figs. 14a and 14b were difficult to see (not shown). If a more sophisticated cloud scheme had been used in this study, it is possible that the additional degrees of freedom allowed might cause polar clouds to be less sensitive to spatial resolution. However, our understanding of the basic mechanism by which the excessive cloudiness is reduced with resolution does not require a role for microphysical processes.

Independent of RAC complications, it is an unrealistic circulation that is a primary explanation for the excessive cloudiness. With both nests active, and with appropriate limits placed on the fraction of dust particles that are allowed to serve as ice nuclei in the polar region, clouds in the OSU MMM are sparse and transient, in good agreement with observations. Central to the GCM RAC issue is the large-scale radiative forcing in the polar region due to the excessive cloudiness that causes more clouds to form. With sparse and thin clouds, as in these simulations, RAC may have very little effect at $L_s = 120°$ during northern polar summertime. To understand the effects of RAC at the mesoscale, it will be implemented in future efforts.

4.2. Winds at high-resolution

Given the complex forcing of topography, albedo and thermal inertia during the $L_s \sim 120°$ season, the circulation is highly complex. Katabatic flow off the polar dome is a basic element of this circulation, and the Coriolis effect steers katabatic winds into

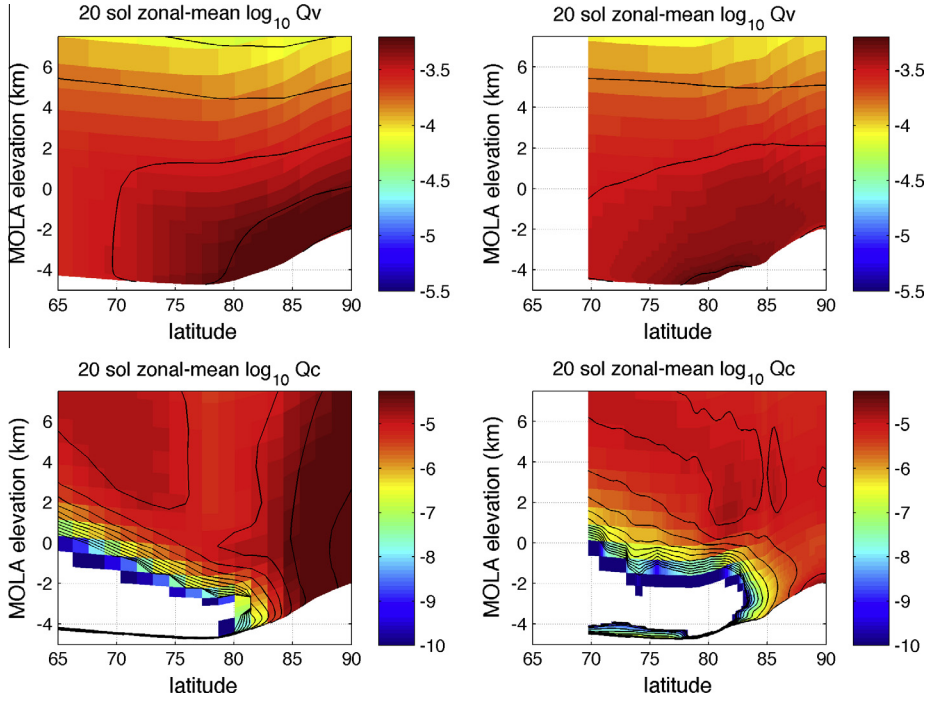

Fig. 14b. Water vapor and cloud ice mass mixing ratios (Q_v and Q_c) are shown for the two cases shown in Fig. 14a.

easterlies on the slopes of the polar dome. The cold polar dome has a larger-scale effect on the meridional structure of atmospheric temperature, causing a baroclinic zone to form in the lower atmosphere that gives rise to transient eddies that have a sizeable effect on instantaneous winds. It follows that easterlies near the surface become westerlies aloft in a weak jet due to the poleward decrease of air temperatures in the baroclinic zone. In the lower atmosphere (below ~10 km AGL), the relatively strong (although rather shallow) transients are influenced by and act to modify winds near the ground. These interactions take place at latitudes of sharp gradients and zonal asymmetries in all of the surface fields. For any location in this region, the interdiurnal variations in the wind field are not small in comparison to the mean diurnal cycle. All of this can basically be deduced from Fig. 15, where the 20-sol diurnal mean wind field and an example of the instantaneous excursion wind field (actual wind minus the 20-sol mean wind at that time of day) are shown for the 15 km nest at two heights above ground (at ~200 m and ~5 km). For comparison, the zonal-mean wind fields are shown in Fig. 14a. In Fig. 15, the 20-sol diurnal mean winds are in the left subplots on a color map of topography; in the right subplots excursion winds are shown on a color map of percentage normalized excursion surface pressure, the quantity $P'_{sfc}(\lambda,\phi,t)$, formed as follows:

$$P'_{sfc}(\lambda,\phi,t) = 100 \times (P_{sfc}(\lambda,\phi,t) - \alpha(t)\bar{P}_{sfc}(\lambda,\phi,hr))(\bar{P}_{sfc}(\lambda,\phi))^{-1}.$$

In this expression, $\alpha(t)$ is a trending parameter constructed by fitting the 20-sol domain mean surface pressure with a low-order polynomial (typically linear), and the quantity $\bar{P}_{sfc}(\lambda,\phi,hr)$ is the 20-sol mean diurnal cycle of surface pressure at each location in the domain. The difference between the instantaneous surface pressure and the trended mean diurnal cycle is normalized by the 20-sol mean of the local surface pressure, $\bar{P}_{sfc}(\lambda,\phi)$. For any single sol, with generally only small trends in the region at this season, the diurnal mean wind field is highly similar to the 20-sol means shown in Fig. 15. A very important exception does exist in the region between the NPRC and the slopes of Alba Patera, and is described below.

Responding to transient surface pressure disturbances, excursion winds near the ground (~200 m AGL in Fig. 15) have amplitudes that are more than half the maximum wind speeds in the model layer. The interdiurnal variability of winds near and across the polar dome is a very important aspect of the circulation, and is sure to cause vigorous meridional mixing. As an important part of the local diurnal cycle of wind, the strongest easterlies near the edge of the polar dome progress westerly following the warmest ground temperatures. At ~5 km AGL, the winds near the edge of the polar dome are predominantly from the west, evidence of the baroclinic zone and the weak jet. Thus, a sizeable wind shear is seen in the lower atmosphere, wherein transient eddies are vigorous and active in modifying the instantaneous circulation. The synoptic structure of these eddies is sensitive to the dust loading and the temperature of the NPRC, as has been seen in previous studies (Tyler and Barnes, 2005; Tyler et al., 2008).

If a realistic interactive dust distribution were used, the synoptic structure would be under constant modification from changes in the atmospheric thermal forcing. However, even without the variations in heating rates that such a scheme would provide, outbreaks of strong flow directly across the polar dome are seen to develop when strong lower wavenumber synoptic structures break down into weaker higher wavenumber structures (Tyler et al., 2008). The complexity and vigor of the polar circulation is very important for the regional complexity and meridional structure of atmospheric water vapor.

Finally, near the location of Phoenix (marked with a white asterisk in each subplot of Fig. 15) a cyclonic structure is seen in the 20-sol mean winds in the region between the NPRC and the northern slopes of Alba Patera. In the right subplots of Fig. 15, we see that the instantaneous excursion winds here are more complex and vigorous when compared to the rest of the domain. What appears to be a stationary eddy in the mean wind field is in reality a circulation that migrates and evolves over the course of this 20-sol period. As discussed in Section 4.4, this circulation has an important role in the formation of an annular cloud in the model, very similar to that described by Cantor et al. (2002).

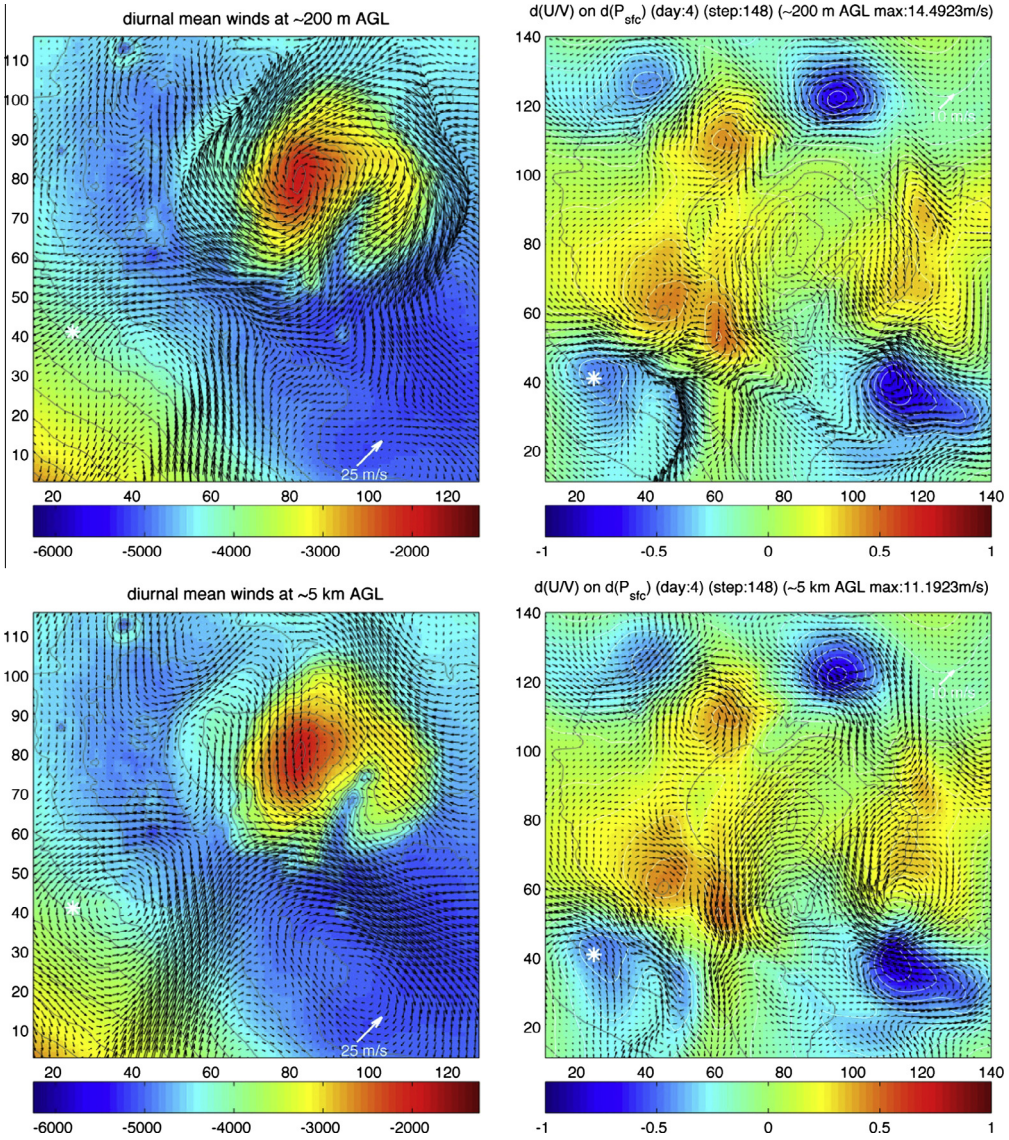

Fig. 15. 20-sol diurnal mean winds (left), and instantaneous excursion winds (right, actual wind minus the mean diurnal cycle value) are shown at two elevations, ~200 m (top) and ~5 km AGL (bottom). The 20-sol mean winds are shown on a color map of topography, and the excursion winds are shown on a color map of the percentage surface pressure excursion amplitudes (see text for definition). The *X* and *Y* axes are labeled with gridpoint numbers from the 15 km nest (to show the transient eddy surface pressure amplitudes clearly, the regions are not identical). (For interpretation of the references to color in this figure legend, the reader is referred to the web version of this article.)

4.3. Water vapor at high-resolution

Shown in Fig. 12a, and as previously noted (Tyler and Barnes, 2011), the greatest ice sublimation rates occur near the edges of the NPRC ices. Responding to the effect that transient eddies have on local winds and the level of atmospheric saturation at a specific location, considerable variability is seen in local sublimation rates from day to day. That the sublimation of ice is greatest along the edges of the largest NPRC ice regions is a consequence of two factors. The first is that winds tend to be much stronger and favorable to equatorward ventilation at these locations, and the second is related to the cold surface of the ice itself. Air over the interiors of these ice regions is cold and tends to remain saturated, a state in which sublimation is unlikely to occur. Forced by the cold surface, inversion is the nominal state of the lower atmosphere over the larger ice regions. If sublimation does occur, vertical mixing is small and the air saturates quickly. Inversions persist over the interior of the polar dome. Moreover, for a sizeable fraction of the polar dome there is a small net accumulation of ice through deposition and fallout (see Fig. 12b). Deposition and snowfall certainly have an effect on the albedo of the NPRC (Malin et al., 2008). The spatial distribution of the vapor column is a consequence of these processes and the winds. With sufficient spatial resolution, the model circulation can more readily ventilate vapor from these locations equatorward. Here we examine the spatial and temporal distribution of water vapor in the polar region at high resolution.

Using case 3 results (described above), maps of the instantaneous vapor column depth are shown in Fig. 16 for two widely separated times in the simulation, one early in the 20-sol period and one late (each is ~8.5 days from the central date of $L_s = 120°$). At both times, the spatial structure is complex, showing that transient eddies have an active role in the transport of vapor, causing strong advection and mixing both zonally and equatorward. The locations of the maxima in the vapor field reveal the importance of winds, and again show that the greatest sublimation occurs at the edges of the polar dome. The right subplot of Fig. 16 is at a later time in the simulation, when overall there is somewhat less vapor in the atmosphere (this is consistent with TES for both MY25 and

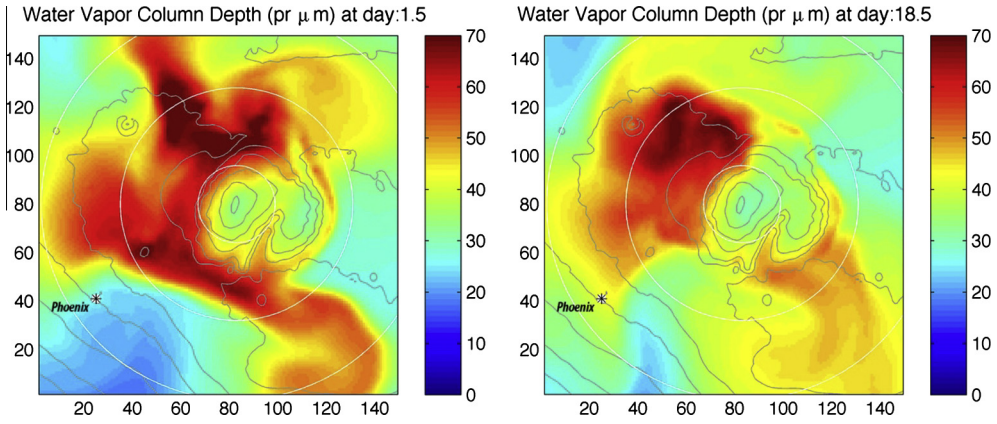

Fig. 16. Column water vapor abundances from the 15 km nest are shown. Two instances from case 3 are compared. The first is 8.5 days before $L_s = 120°$, while the second is 8.5 days after $L_s = 120°$. The location of Phoenix is identified and the nest topography is contoured at intervals of 500 m. The *X* and *Y* axes are labeled with gridpoint number and latitude circles are drawn at 65°, 75° and 85°N.

MY26). The zonal-mean profile of the vapor column shown in Fig. 8 was constructed using 10 sols centered on $L_s = 120°$, a period when both the model and the TES observations show very little trend. In the left subplot of Fig. 16 (early in the simulation) the atmosphere above Phoenix is dry, with only ~25 pr μm of water vapor, much less than the zonal-mean at this season, ~40 pr μm. Later in the simulation (right subplot) the vapor column over Phoenix is much larger, ~45 pr μm. Transient disturbances associated with the high latitude baroclinic zone are sure to be involved in the instantaneous vapor distribution, and their influence can be seen in both subplots of Fig. 16. A complete explanation for the change seen at Phoenix must include the changing circulation that is suggested by the 20-sol diurnal mean winds in the left subplots of Fig. 15.

Early in the simulation, this circulation contributes to the advection of water vapor to the southwest of Phoenix. The strong poleward flow that is part of this circulation (to the east of Phoenix in Fig. 15) is dry air. Because of the state of the circulation at this time, the atmosphere to the southeast and over Phoenix stays much drier than the expected zonal-mean value. As the simulation progresses, the strong poleward flow (and the dry air region) migrates to the east, and the vapor column over Phoenix begins to grow larger. The circulation also moves poleward, and with this change the cyclonic structure of the circulation appears to assist in the advection of vapor over Phoenix from the west.

Since clouds are not radiatively active, model dynamics remain essentially unaffected by water mass, which causes the circulation to be the same in all five cases described and explored in Section 3.4. However, the vertical distribution of water mass (and thus its horizontal advection by the winds) is a consequence of the values of f_{IN} and f_{SED}. Since f_{IN} controls the number of cloud particles, it affects the rate of change between ice and vapor in an air parcel, thus the mass distribution between the two phases as a function of time. Our model results are more sensitive to f_{IN}, where f_{SED} serves primarily to enhance fallout in compensation for the single particle size carried in the model. When comparing the five cases described in this study, the spatial distribution of the vapor column varies at high latitudes because of these two parameters. Over Phoenix, the differences can be significant, with the greatest differences between cases 3 and 4. Thus, especially for locations near the sharp meridional gradient in the vapor column, the vapor distribution is sensitive to the prescription for f_{IN} (see Fig. 9a).

4.4. The observed recurring annular cloud

In an earlier study, Tyler and Barnes (2005) described a "storm zone" that forms on the northern slopes of Alba Patera. For the three dates that were studied in that work ($L_s \sim 120°$, $L_s \sim 135°$ and $L_s \sim 150°$), the "storm zone" formed only in the $L_s \sim 135°$ case. Since each case used the same very simple dust prescription, this suggests that the dynamical state that produces this "storm zone" is short lived and dependent primarily upon changes in insolation with season. The diurnal heating pattern is dependent on the subsolar latitude, and especially so in the presence of large topography. In this region, the dynamical forcing is a superposition of many competing factors. Model results appear to show that western boundary currents, topographically excited large-scale thermal circulations and strong slope flows are all involved. When this "storm zone" exists, transient disturbances are seen to form high on the northern slopes of Alba Patera. Typically these disturbances are of moderate strength, and move poleward through the "storm zone" to dissipate in higher latitudes. Over the course of a single simulation, one disturbance can form that grows very strong and survives to reach the latitudes just south of the NPRC somewhat to the east of Phoenix. Tyler and Barnes (2005) suggested that the transient disturbance that does this is involved with the recurring annular cloud first described by Cantor et al. (2002). The location and size of these strongest transients is consistent with the annular cloud (Malin et al., 2008), although the date of its simulation ($L_s = 135°$) is too late by ~12° of L_s. In this study, the dust opacity and Conrath-Nu parameter are functions of latitude, the result of a tuning process that yields good high latitude agreement with observations of atmospheric temperature (see Figs. 1 and 3). In this study a similar "storm zone" appears at an earlier seasonal date that is consistent with the appearance of the annular cloud.

A map of the mean strength of surface pressure excursions can be used to identify the "storm zone". By taking the Root Mean Square (RMS) of the percentage normalized surface pressure excursions, defined above as $P'_{sfc}(\lambda, \phi, t)$, the mean transient eddy strength is constructed as follows:

$$\overline{P}'_{sfc}(\lambda, \phi) \equiv \mathrm{SQRT}\sum_{t=1}^{t=N}\left[\left(\frac{1}{N}\right)\left(P'_{sfc}(\lambda, \phi, t)\right)^2\right].$$

Since a larger regional picture is required, 20 sols of surface pressure from the first nest (45 km) are used to construct Fig. 17. At ~110°W, a region of strong transient activity is seen to extend from the edge of the polar dome towards the summit of Alba Patera. This is the "storm zone". Additionally, it is a boundary between a region of negligible transient activity to the west and one of moderate transient activity to the east. When winds in the regions to the east and west are examined at many levels, and over all 20 sols (not shown), it becomes clear that this "storm zone" is also a boundary between two very different diurnal wind regimes.

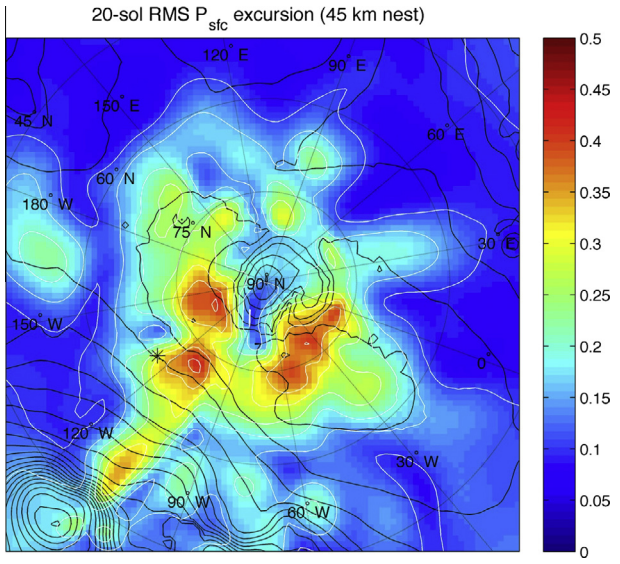

Fig. 17. The 20-sol mean strength of the percentage excursion from the mean diurnal surface pressure cycle is shown (equation in text). Results are centered on $L_s = 120°$, and shown for a subset of the 45 km nest (first modeling nest). The summit of Alba Patera is at the lower left corner and the NPRC polar dome is at the center (as identified by contours of topography). The "storm zone" (as discussed in the text) is seen on the poleward slopes of Alba Patera.

To the west, winds near the surface exhibit a highly repeatable diurnal cycle of clockwise rotation with strong late afternoon upslope flow. To the east, the diurnal cycle is much less pronounced, with winds primarily from the east and strongest in the late afternoon. The "storm zone" between these two regimes is also a convergence zone, which can be seen at both levels in the 20-sol diurnal mean winds of Fig. 15, ~200 m and ~5 km AGL. In part, the "storm zone" is a region of strong transient activity due to the fact that the convergence zone moves eastward during the 20-sol period. Its movement affects the mean diurnal surface pressure cycle differently than a transient eddy does. Examining afternoon convective boundary layer (CBL) depths shows significant variation across the "storm zone" (not shown). Since differing CBL depths have different vertical profiles of air temperature, the resulting differences in the mass of the air column will change the diurnal cycle of surface pressure as this boundary moves to the east. Surrounding the polar dome in Fig. 17, the sizeable $\bar{P}'_{sfc}(\lambda, \phi)$ values are produced by transient eddies. The sizeable "storm zone" values appear to be caused by both transients and the evolving circulation.

An examination of the diurnal mean wind field for all 20 sols reveals the migration and evolution of an underlying structure in the regional circulation. Later in the simulation, directly relating to the formation of the annular cloud, a large disturbance develops along a convergence zone in this structure, which grows into a strong transient that migrates into the most polar latitudes just off the polar dome. When this strong transient interacts with the high latitude vapor field, an annular cloud forms in the model. To depict this event, six instances of the diurnal mean wind field are shown in Fig. 18 (the winds are at ~1 km AGL, with wind vectors shown for every other gridpoint on a color map of wind speed). The convergence zone appears as a low wind speed region (blue) in the midst of stronger winds.

The upper subplots of Fig. 18 show sols 1 and 8, where two changes are seen to occur: (1) the convergence zone moves eastward (for reference a dashed white meridian is drawn) and (2) the northernmost part of the circulation advances toward the pole. The poleward flow of dry air from the south is not shallow, and as the winds turn to the west it is the advection of this dry air into the region that causes the air column over Phoenix (the white asterisk) to remain much drier than other longitudes. In the lower right of each subplot, strong flow is seen to wrap around the eastern flanks of Tharsis; this flow interacts with and affects the convergence zone. It is notable that the strongest flow is seen on the east faces of the topographical features of Tharsis. This is very suggestive of a western boundary current, or that the stronger poleward flow on the east faces develops because of a large-scale cyclonic thermal circulation (forced by Alba Patera and Tharsis). Maybe both circulations contribute to strengthen the flow. Later, for sols 12 and 15 (in the middle two subplots of Fig. 18), the convergence zone is further eastward, while the most northern part of the circulation is further poleward. By sol 15 the most poleward part of the strong flow is beginning to merge into the polar easterlies. As wind directions suggest, column vapor amounts over Phoenix are rising at this time. The flow that wraps around the eastern flanks of Tharsis has become stronger, and is presumably affecting (deforming) the convergence zone. By sol 18, a sizeable perturbation has developed along the convergence zone, which grows into a large cyclonic transient. By sol 20, this transient eddy has migrated up to the edge of the polar dome itself, and is in direct interaction with the sharp meridional gradient in the vapor column.

This is all best seen in an animation (*see supplementary online materials*). It is at this point, near the very end of the simulation, the annular cloud is seen in the morning ice column depths. For an example of actual observations, two occurrences of the annular cloud are shown in Fig. 19a (from Malin et al. (2010), five occurrences are shown in their Fig. 35). The size, location and season of appearance of the annular cloud are surprisingly repeatable from year to year, although each occurrence is distinct from previous years in terms of its longitudinal extent and the amount of structure/texture in the cloud itself. As observed by MARCI on September 3, 2008 during the Phoenix mission, the annular cloud appeared at $L_s = 121.9°$ (Bruce Cantor, personal communication, 2013). The precise timing of its appearance in 2008 is actually quite important, since the annular cloud appears to be dynamically related to other observations made in situ during a very short seasonal window.

In the model, for a local solar time at Phoenix of ~0730, maps of the vapor column depth, the ground temperature, and the ice column depth are shown in Fig. 19b for both the first and second nests (45 km and 15 km resolutions). The annular cloud can be seen in the ice column depths of the bottom subplots. The water vapor column depths in the top subplots reveal the important structure that allows the annular cloud to form. At the 15 km resolution, some internal structure/texture is seen in the cloud that is similar to features seen in Fig. 19a (or Malin et al. (2010), Fig. 35). In the vapor column, the overall structure is much like an occlusion that sometimes forms with a mature terrestrial cyclone, where the air mass boundary has wrapped around on itself. At this stage in the simulation, when the cloud is most clearly resolved in the model, the clear central region of the annular cloud is not the exact center of the surface pressure minimum. The explanation for the clear central region is the structure in the water vapor field; it is not the result of very strong dynamics such as with a terrestrial hurricane. The formation of the annular cloud in the model is best seen in an animation of the vapor and ice column depths over the course of the simulation (*see supplementary online materials*).

The rapidly evolving circulation shown in Fig. 18 (that is responsible for the annular cloud) has a complex forcing. We believe three factors are important: (1) a large-scale topographically driven thermal circulation, (2) a western boundary current and (3) strong slope flows. The dust prescription that was used in this study improved model agreement with observed air temperatures. This serves to explain why the "storm zone" (and the

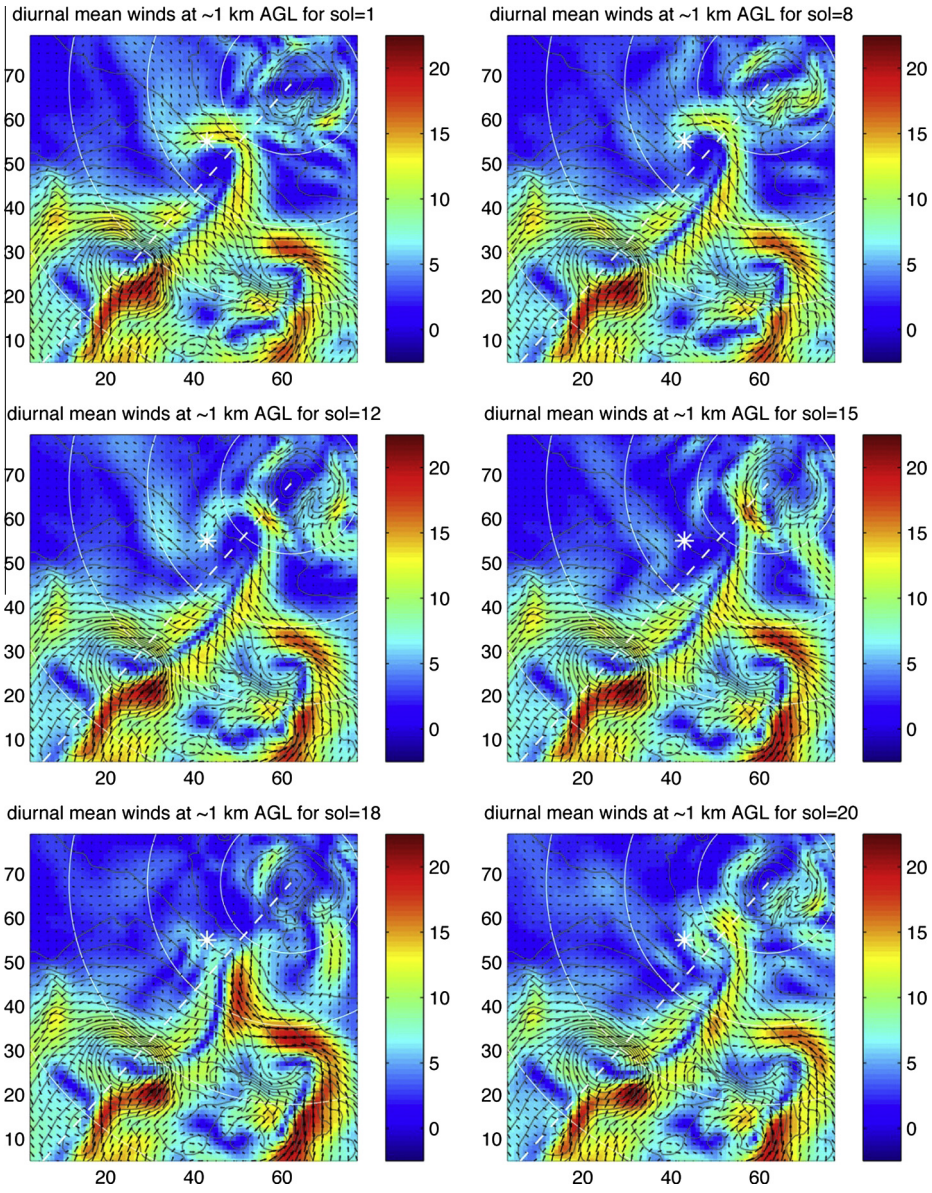

Fig. 18. Six instances of the diurnal mean wind field at ~1 km AGL are shown (sols 1, 8, 12, 15, 18 and 20). Wind vectors are shown for every other location for a subset of the 45 km nest (115 × 115 total size). The location of Phoenix is shown with a white asterisk, and topography is contoured at 500 m intervals. A white dashed meridian is added to better reveal movement of the circulation, and thin white lines are parallels at 30°, 45°, 60° and 75°N. The *X* and *Y* axes are labeled with gridpoint number.

annular cloud) now occurs in the correct seasonal window. This supports the notion that the large-scale thermal structure plays a key role through (1) and (2) above. If a number of mesoscale simulations of the same duration were performed (overlapping, and for a somewhat different L_s range), the synoptic structure of high latitude transient eddies would be different for any single L_s value in these simulations. In such an experiment, the importance of the synoptic structure in relation to the importance of the state of the rapidly evolving circulation on the poleward slopes of Alba Patera could be investigated. It is possible that a specific synoptic structure serves as a "trigger" for the disturbance that grows into the large transient and causes the annular cloud to form. Seemingly, a great deal of variability would be expected in the instantaneous synoptic structure from year to year. Smaller transients do move poleward through the "storm zone", and these might also serve as a "trigger" mechanism that excites the large disturbance along the convergence zone. For these smaller transients, very little effect is seen in the diurnal mean winds of Fig. 18.

It is possible that this rapidly evolving structure in the circulation produces only one large and strong transient each year, and this transient is then responsible for the annular cloud that forms seasonally each MY. So far, our modeling has not produced more than one very large transient in a single simulation. After this one large transient forms, the possibility of another such event may be lost as the convergence zone moves off to the east and the "storm zone" disappears for the year. Even with the "storm zone" being seen only in the $L_s = 135°$ case of Tyler and Barnes (2005), the movement of the convergence zone across the northern slopes of Alba Patera to the east was seen in the three dates simulated (Fig. 6 of Tyler and Barnes (2005) compares 20-sol mean winds at ~1 km AGL for all three simulations). Certainly, a more thorough study of the dynamics involved is needed. All three of the climate "cycles" on Mars are at play (CO_2, dust and water), and with $L_s \sim 120°$ a season where the state of these "cycles" is highly repeatable from year to year, the recurring annular cloud is a phenomenon that is useful for model testing and validation.

4.5. Profiles of vapor and particle size over Phoenix

As seen in Figs. 9b and 9c, the fraction of dust particles allowed to become ice nuclei (f_{IN}) has a sizeable effect on the ice column depth in the polar region, as well as on the mean size of cloud particles (Fig. 11). For high northern latitudes, smaller values (~5%) cause the zonal-mean of the visible cloud ice opacity to agree quite well with observations (Fig. 10). As simulated by Daerden et al. (2010), the fraction of dust particles that nucleate is typically a few percent. Sufficient spatial resolution appears to be important for this result (Figs. 13, 14a, and 14b), and unrealistic cloud scheme parameters would be required otherwise. The formation of larger particles is a key aspect of simulating the observed vertical structure of ice over Phoenix. The Phoenix LIDAR observations (Whiteway et al., 2009) provide direct observation of ice particle sizes and the height of cloud ice above the ground, and help to further constrain model results.

As a function of time and elevation above the ground, vertical profiles of atmospheric vapor and cloud particle size over Phoenix are shown in Figs. 20a (cases 1–3) and 20b (cases 3–5) (all cases are described in Table 1). In Fig. 20a, with f_{IN} changing from a constant 50% in case 1 to the weakly limiting prescription in case 2 (see Fig. 9a), no change is seen in the vapor mixing ratio profiles. With f_{SED} changing from 1.25 to 1.75 (case 2 to case 3), atmospheric vapor is still unchanged. From case 1 to case 2, ice particles grow larger, with the largest particles reaching ~15 μm versus ~10 μm. With f_{SED} larger in case 3, Fig. 9b shows that column ice amounts at high latitude become smaller, which requires somewhat smaller cloud particles since the number of particles is prescribed in the model and the same in both cases. Because of this, f_{IN} is central in controlling cloud particle size.

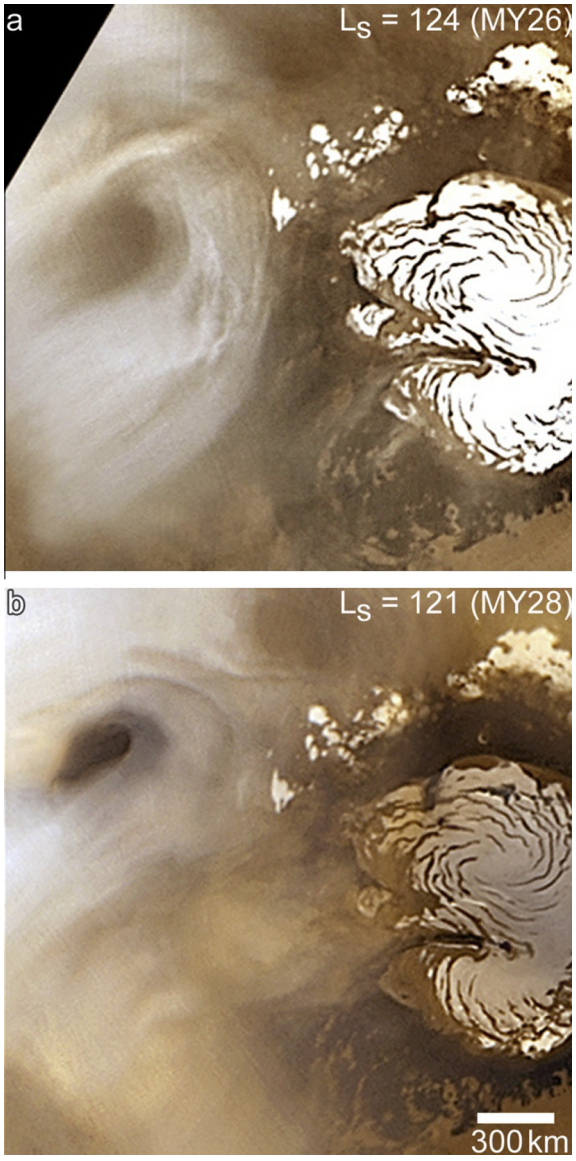

Fig. 19a. Two different occurrences of the annular cloud are shown, from MY26 and MY28. Images are wide-angle MOC. For reference, see Malin et al. (2010) Fig. 35.

In Fig. 20b, the color range is doubled to show the larger particles that form in cases 4 and 5. Fig. 9a shows that at Phoenix (~68°N) the value of f_{IN} is 35% for case 3, 5% for case 4 and 2.5% for case 5. With the much stronger limiting of f_{IN} in cases 4 and 5, the time evolution of the vapor column is modified in comparison to cases 1–3. A delay in the increase of the vapor mass mixing ratio over Phoenix is seen. Since, in response to the changing regional circulation, vapor is actually being advected over Phoenix via a circuitous path (from the WSW), stronger limitations on f_{IN} have an important effect on the resulting horizontal and vertical structures of vapor and ice at Phoenix. The larger particles that form in cases 4 and 5 fall faster and further, changing the vertical structure of water mass and causing the bottom of the cloudy layer to appear (by sol 15) at ~5 km AGL versus ~6 km AGL in case 3. In the morning over Phoenix, cloud particles grow to ~25 μm in case 5, sizeable for a mean (single) particle size. Fallout has an important role in the vertical structure of water mass, and the winds in turn modify the horizontal structure, the result being that the increase in the vapor mass mixing ratio is delayed in cases 4 and 5. Due to the complexity of the circulation the net effect is not obvious, and much larger vapor mixing ratios are seen shortly after the slower rise in cases 4 and 5. Somewhat similar to these effects, the formation of the annular cloud is adversely affected in cases 4 and 5 in comparison with case 3 (not shown). For the annular cloud, cases 1–3 provide the best "looking" examples, while case 3 provides the best fit to the zonal-mean opacity in Fig. 10.

In all five cases clouds do not form below ~10 km AGL over Phoenix until later in the simulation when the water vapor column peaks at ~45 pr μm (after sol 15). The increase in the vapor column is a consequence of the evolving circulation, as seen in Figs. 16 and 18. As the simulation passes through L_s = 120° (sol 10 in Figs. 20a and 20b), water vapor that had previously been advected to the SW of Phoenix is now caught up in the circulation and is advected over Phoenix. An animation shows the diurnal and seasonal changes (*LinkToAnimationTwo*), as well as the structure of daily pulses of newly sublimated vapor that get advected away from the edge of the polar dome. By day 15, with far more vapor in the column over Phoenix, clouds form nearer the ground in all cases. If the time axis is expanded to show just the last five sols, we see (in the slanting path with time for the largest particles) that fallout plays a significant role in bringing ice much closer to the ground. Also, although difficult to see in Figs. 20a and 20b, "fog" forms in the lowest ~3–5 model layers at night, and reaches depths of ~100–150 m before it evaporates in the morning. The structure of this "fog" is more easily seen in the rapid decrease in the mass mixing ratios of vapor in the left subplots.

With the rapid decrease of cloud heights over Phoenix, factors other than a gradually increasing vapor column are likely to be at play. When vertical slices through the ice particle size field over Phoenix are examined, the cloud ice that appears in the AM at lower levels develops along with new structure in the slice. Since clouds do not grow steadily towards the equator and the surface to cover Phoenix with the increasing vapor column, transient dynamics are likely to be involved. For both AM and PM times of day (~0230 and ~1430 LTST), slices through the cloud particle size

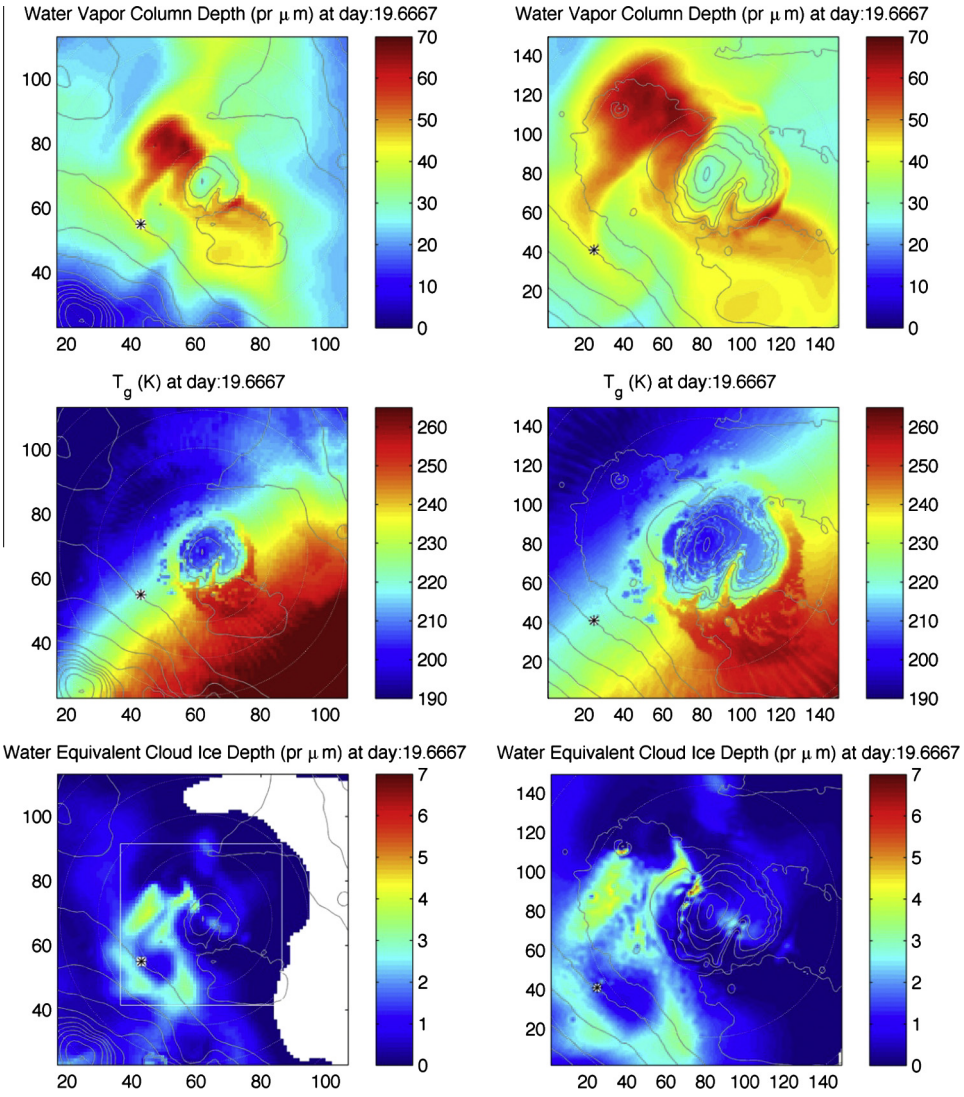

Fig. 19b. Maps of column vapor abundance, ground temperature and column ice abundance are shown for the first and second nest (45 km and 15 km resolutions) at ~0730 AM LTST from case 3. An annular cloud, as modeled in this study, is shown in the lower subplots. The location of Phoenix is marked in each subplot, with gray contours of topography drawn to help orientation. The *X* and *Y* axes are labeled with gridpoint number.

field of case 3 are shown in Figs. 21a (sol 5) and 21b (sol 15). The upper subplots show ice particle sizes in the lowest model layer ("fog") for the AM (left) and PM (right) local solar times at Phoenix. Vertical slices are shown in the lower subplots (the surface transect of the slices is shown with a dotted black line in the upper subplots). In the vertical slices, AM clouds at lower levels are only seen over Phoenix in Fig. 21b (day 15). An animation of the cloud ice column reveals that these clouds appear due to advection from the WSW. Moreover, the cloud ice seen in the afternoon over Phoenix in Fig. 21b provides some additional evidence that dynamics are involved in other ways than simply the advection of water into the column over Phoenix.

Comparing cases 3 and 4 in Fig. 20b shows that the vapor columns evolve quite differently, which means results are sensitive to the cloud scheme parameter f_{IN}. Because the circulation is complex, the response to this sensitivity is spatially complex. Near Phoenix, $L_s \sim 120°$ is a season of change, and with the vigor of the circulation, dynamics must at times have a significant role in cloud formation. In these simulations, a strong cyclonic disturbance modifies the regional circulation; its effect is readily seen in the time change of the vertical profiles of modeled winds over Phoenix (not shown). The Phoenix surface pressure record in Fig. 7 is clear evidence of a strong transient disturbance nearby; a sizeable excursion in the surface pressure record that occurs at $L_s \sim 120°$ (spanning sol 94). This occurs just prior to the lower-level clouds seen by the Phoenix LIDAR ($L_s = 122°$), which suggests these two observations are related and dynamics are involved. As noted by Moores et al. (2010), this period was particularly active for clouds moving in different directions at multiple heights AGL. Similar and rapid changes in cloud heights were simulated in this study (even with the highly simplified microphysics), which is unlikely if dynamics are not involved. At Phoenix, the dust opacity observed by LIDAR decreased by a factor of three (Whiteway et al., 2009); with fewer dust particles, larger cloud particles would form and fall closer to the ground. In the OSU MMM, dust particle number densities are independent of dynamics, although rapid changes in the wind field reveals the proximity of a strong transient circulation.

The strong transient simulated in the model does not pass directly over Phoenix, which the modeled surface pressure record in Fig. 7 shows. However, an examination of surface pressure maps shows that it passes near Phoenix (~500 km to the east moving poleward). An examination of the Phoenix telltale winds (Holstein-Rathlou et al., 2010) was carried out to try and identify

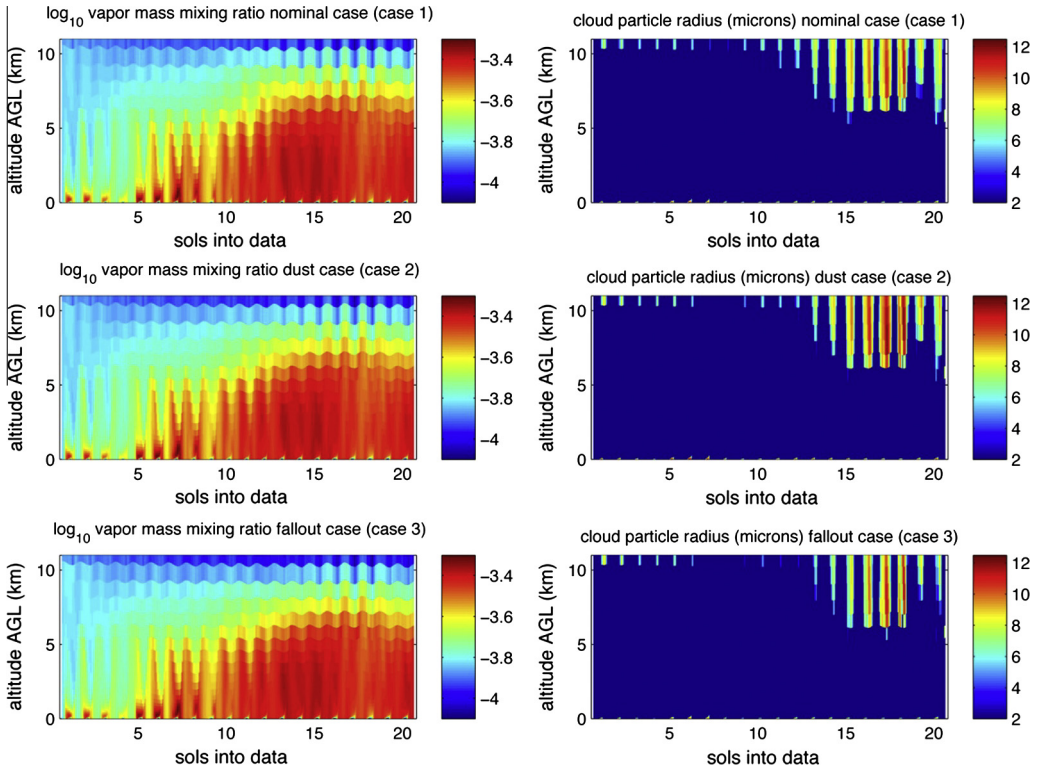

Fig. 20a. For the 20-sol analysis period, the vertical structure of the water vapor mass mixing ratio and the size of ice particles over Phoenix is shown for cases 1–3 (top to bottom).

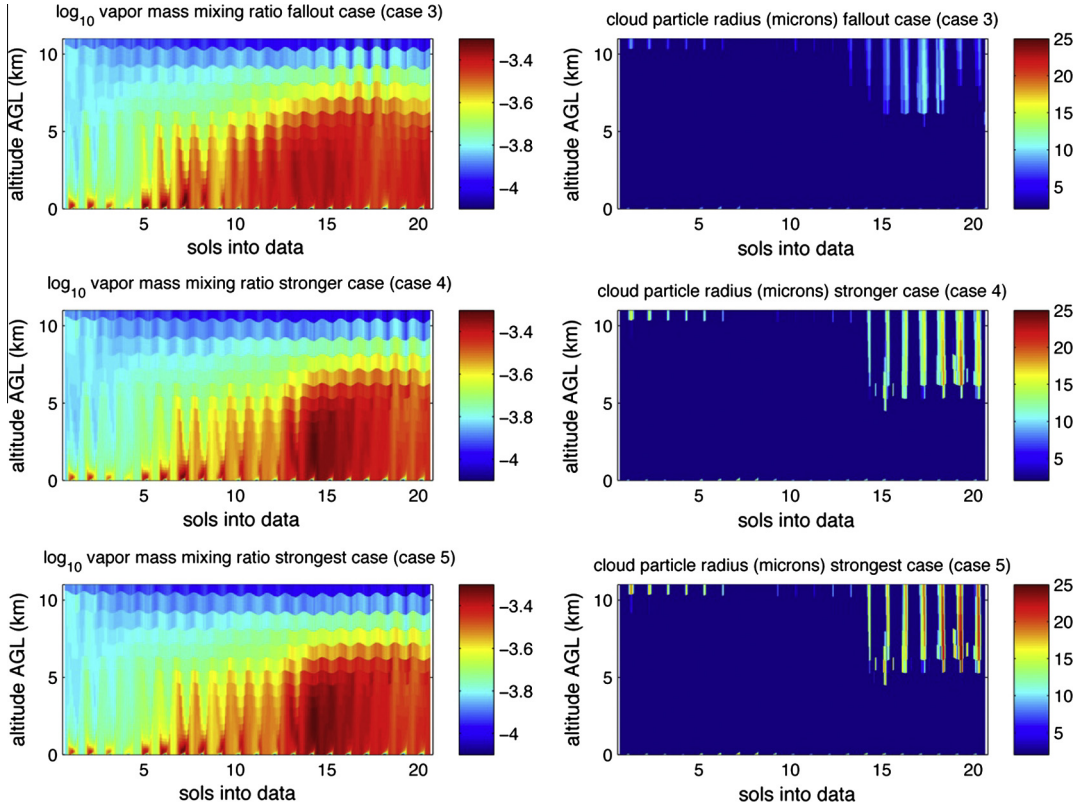

Fig. 20b. For the 20-sol period, the vertical structure of the water vapor mass mixing ratio and the size of ice particles over Phoenix is shown for cases 3–5 (top to bottom).

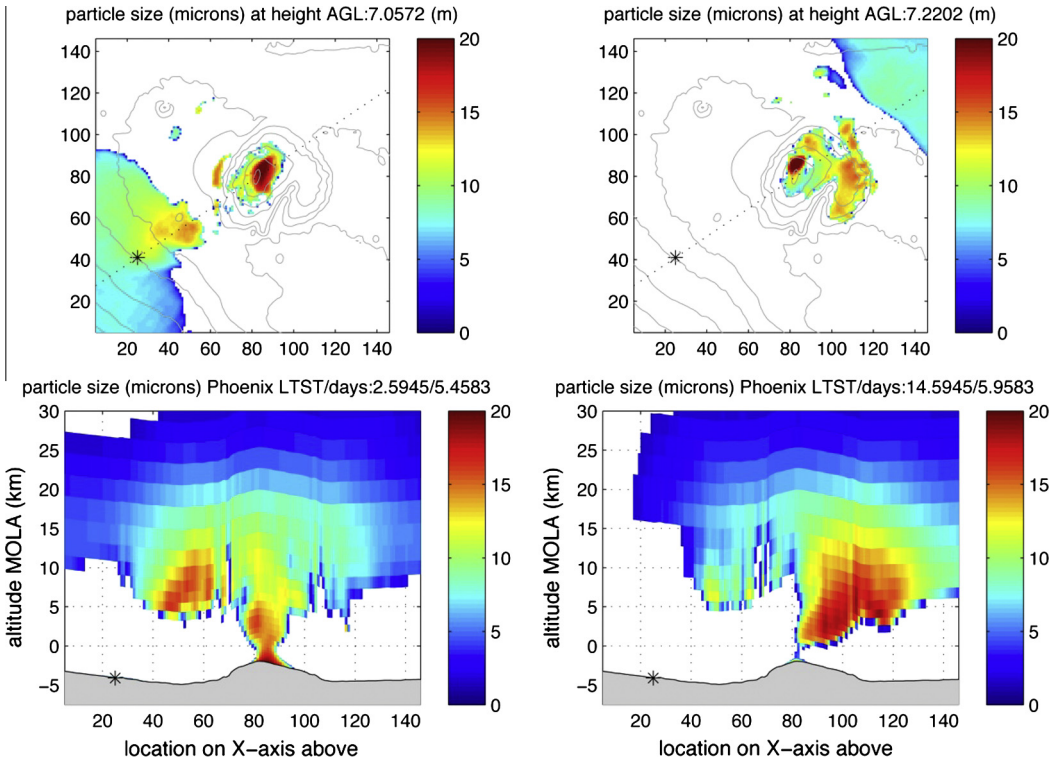

Fig. 21a. Vertical slices of cloud particle size are shown in the lower subplots for day 5 from the 15 km nest of case 3 at ~0230 and ~1430 LTST. Values for LTST and the day are shown in the subplot titles. The black asterisks indicate the location of Phoenix. The surface transect of the slices (dotted black line over Phoenix and the pole) is identified in the upper subplots (horizontal slice), where the particle size in the lowest model layer (ground fog) is shown for the same LTST/day as the subplot below. Contours of model topography are drawn at 500 m intervals in the upper subplots. In the upper subplots, the *X* and *Y* axes are labeled with gridpoint number.

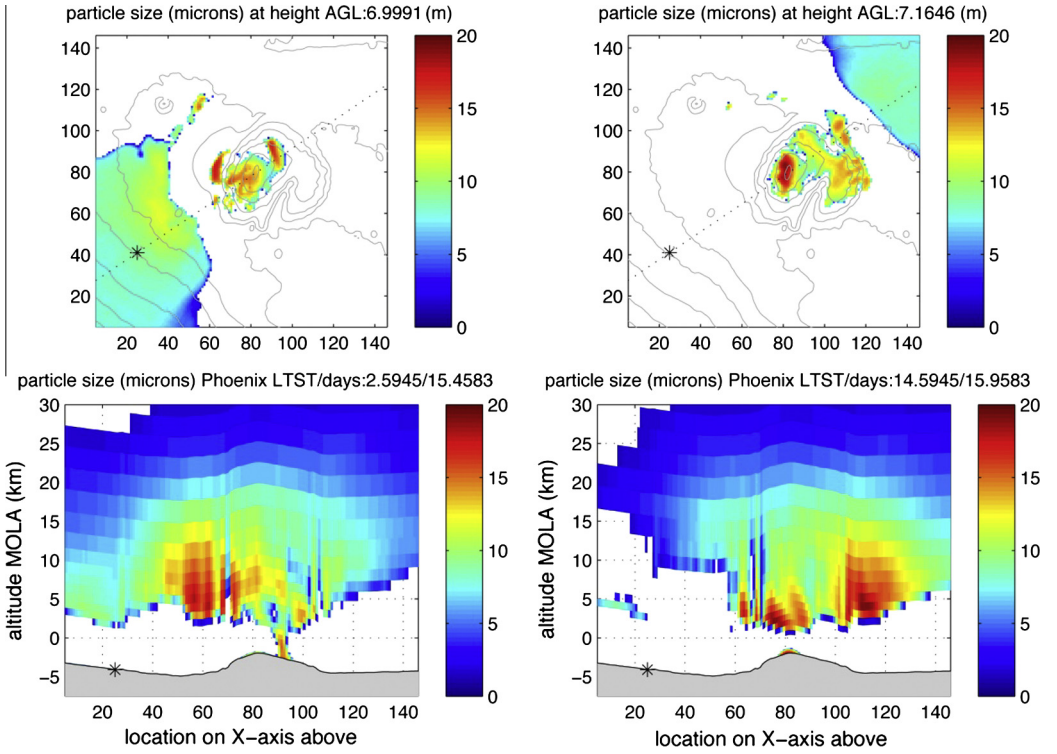

Fig. 21b. Vertical slices of cloud particle size are shown in the lower subplots for day 15 from the 15 km nest of case 3 at ~0230 and ~1430 LTST. Values for LTST and the day are shown in the subplot titles. The black asterisks indicate the location of Phoenix. The surface transect of the slices (dotted black line over Phoenix and the pole) is identified in the upper subplots (horizontal slice), where the particle size in the lowest model layer (ground fog) is shown for the same LTST/day as the subplot below. Contours of model topography are drawn at 500 m intervals in the upper subplots. In the upper subplots, the *X* and *Y* axes are labeled with gridpoint number.

where the strong transient associated with the Phoenix surface pressure record at sol 94 was in relation to the lander. The telltale observations reveal that much stronger winds existed during sol 94, although an attempt to determine the location of the transient system relative to Phoenix (due to change in the wind direction) was inconclusive (C. Holstein-Rathlou, personal communication, 2014). Certainly, the Phoenix winds are highly variable across the $L_s \sim 120°$ season. It is also fairly clear from this data set that wind speeds and directions are undergoing a seasonal transition, as shown in Figs. 14 and 16 of Holstein-Rathlou et al. (2010).

For the $L_s \sim 120°$ season, it is worth noting that the very low clouds and persistent ground fog seen over the polar dome are regular features of the circulation. In Figs. 21a and 21b, we see that cloud ice can exist all day throughout the entire lower atmosphere over the polar dome. This reinforces a key conclusion of this study, that air over the interior of the polar dome is typically saturated. As a result of fallout and the direct deposition of vapor onto the cold surface of the polar dome, ice that sublimates from the periphery into the atmosphere can be returned to the NPRC through sporadic flow over the pole (caused by transient eddies). This may have climatological significance, although in comparison to the sublimation rate for the NPRC it is not large (~6% of NPRC rate, see Fig. 12b). Near the surface over the central region of the polar dome, inversion is the nominal state of the atmosphere, so there is little vertical mixing near the ground. For NPRC ices (the polar dome especially), sublimation of ice into atmospheric vapor occurs primarily along the periphery. This vapor is readily mixed equatorward due to the strength and inter-diurnal variability of the winds, and sufficient resolution appears to be required for the simulation of these key processes.

Although case 3 is the best match to the TES opacity observations, examining AM clouds over Phoenix in cases 4 and 5 at sol 15 is useful for showing how the strongest limiting prescriptions for f_{IN} affect the size of cloud particles and the structure of ice in the vertical slice. For cases 4 and 5, the AM vertical slices are shown in Fig. 22 for sol 15. Compared with case 3, much larger cloud particles are seen (a wider colorbar is used in Fig. 22). The value of f_{IN} is smallest in case 5 over Phoenix (2.5%), and in response to the many factors involved, cloud particles grow to ~25 μm in the AM. Significantly larger particles have certainly been observed (Whiteway et al., 2009), while a recent study suggests that particle sizes of ~25 μm may actually be fairly typical in the northern polar summertime (Lemmon, 2014).

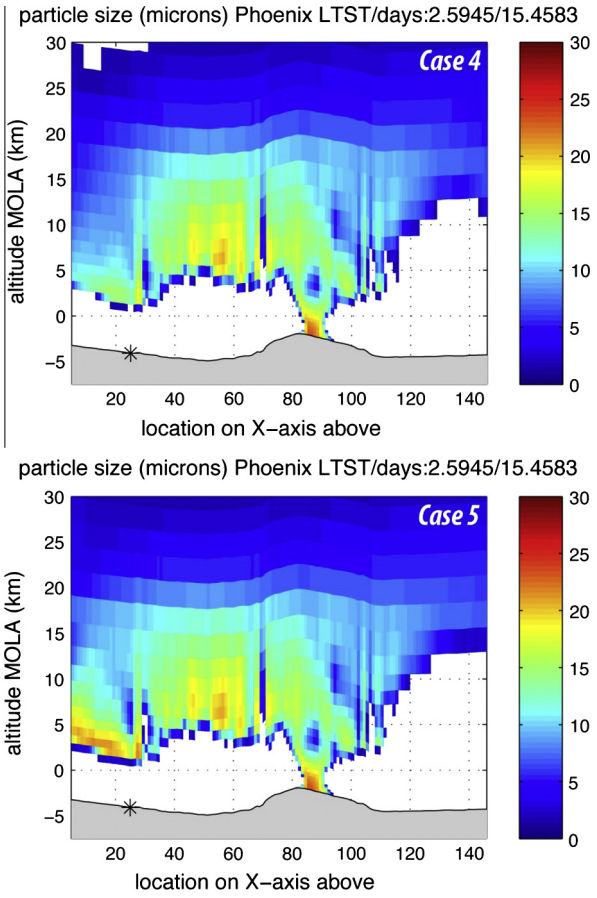

Fig. 22. Vertical slices of cloud particle size are shown for cases 4 and 5 for the AM time of sol 15. The slice is identical in location and time with those in the AM subplots of Figs. 20a and 20b.

5. Summary and conclusion

The OSU MMM was used to study water vapor and water ice clouds during northern polar summertime (the $L_s \sim 120°$ season). This season is extremely important in the annual water cycle. At larger scales it is a time of small trends, where the vapor column at high latitudes remains very near the annual maximum; it is also a time of minimum cloudiness over the polar region. This combination has proven to be quite challenging for GCMs. Typically, far too much cloud ice is simulated over the polar region, and when more sophisticated cloud schemes are utilized (especially schemes that include RAC), the clouds are even thicker and the models exhibit a great deal of sensitivity to poorly constrained parameters. There is much to learn about the formation of water ice clouds on Mars, and high-resolution modeling needs to be an important part of this process. In an environment as complex as the NPRC region, where sharp gradients are the norm (in topography, albedo, thermal inertia and certainly in ground temperatures), the dynamics cannot be sufficiently realistic unless the very complex environment itself is sufficiently resolved. Tuned to the $L_s \sim 120°$ season, with two levels of nesting to a spatial resolution of ~15 km over the polar region, we investigated the importance of spatial resolution and examined mesoscale aspects of the seasonal water cycle. In good agreement with independent observations, the dynamics that lead to the formation of an annular cloud in the model atmosphere are examined. Compared with observations gathered during the Phoenix mission, we find very good agreement with model results. There appears to be an important seasonal transition in the Phoenix region at $L_s \sim 120°$. Changes in the regional circulation appear to be largely responsible, and the seasonal appearance of the recurring annular cloud (Cantor et al., 2002) may mark this transition.

A great deal of effort was invested in producing realistic dynamics at the mesoscale. New albedo and thermal inertia data were developed to resolve the complexity of the NPRC region. The construction of these new data used imagery and publicly available data. Location information and "raw" albedo data are taken from imagery (Wendy Calvin, personal communication, 2009), while final albedo values are guided by the publicly available data of Putzig and Mellon (2007). A number of iterations were used to refine these newly constructed maps. In comparison with TES observations, simulated AM and PM ground temperatures at $L_s \sim 120°$ in the NPRC region are almost everywhere within ~5 K of observations at a resolution of ~15 km (see Fig. 6). Presumably this helps greatly towards a realistic dynamical simulation, as well as a realistic depiction of locations that are able to sublimate ice into atmospheric vapor.

A good mesoscale simulation requires realistic boundary conditions, both lateral boundaries for the mother domain and physics that give the model realistic source/sink terms in the exchange of water mass between the surface and the atmosphere. The cloud

scheme of Montmessin et al. (2004) was incorporated into the OSU MMM, with a surface reservoir added to keep track of ice that falls to the ground (snow) and vapor that is directly deposited when temperatures drop below the frost point (frost). Ice in this surface reservoir is free to sublimate back into the atmosphere when conditions allow. With this model functionality, the result is a simulation where the atmospheric vapor column remains in very good agreement with observations for the duration of the simulation. This is not a given for a 30 sol run, as many poorly constructed initializations revealed. If a mesoscale model is to be used to improve our understanding of the water cycle, it is very important that it does a good job in capturing the larger-scale aspects of the water cycle. It seems only from that starting point that investigations into more subtle aspects of the water cycle can be carried out. Efforts here preface future studies at seasons when sizeable secular trends in the atmospheric state must be realistically simulated.

A parameter sensitivity and model tuning exercise was performed to determine how the meridional structure of clouds in the model responds to (1) the fraction of dust particles that are allowed to become cloud particles (f_{IN}) and (2) the degree to which the sedimentation velocity is enhanced in the cloud scheme (f_{SED}) (to account for larger particles if a size distribution was used). With realistic limitations for f_{IN} in polar latitudes (~3–5%), the visible opacity of ice in the model atmosphere is in good agreement with observations. Simulations with various meridional profiles of f_{IN} suggest that much larger nucleation fractions are required for the realistic simulation of clouds equatorward of the polar region. It may be useful to think of cloud formation as occurring in two modes at this season: (1) a polar mode with small diurnal meteorological cycles and only moderate dynamical forcing and (2) a lower latitude mode with large diurnal meteorological cycles and strong dynamical forcing. In the balance between environmental forcing and microphysical processes, smaller supersaturations would be expected in the polar mode. With so much water vapor and only very small ice opacities observed, the summertime polar atmosphere is unique. Recent observations suggest that larger (~25 μm) ice particles may be typical in the polar summertime. It may be that small supersaturations causing low rates of nucleation (in an environment with a great deal of vapor available) is the explanation for these larger ice particles. We note that larger particles allow for a significant amount of ice the polar atmosphere without the opacity becoming large.

When the model is run without nests (which lowers resolution over the pole from 15 km to 135 km), the mass of cloud ice in the polar atmosphere increases tenfold. Because of this, it appears that at least some of the problem GCMs have with excessive cloudiness and sensitivity during northern summertime is caused by insufficient spatial resolution. In this study, it is the activation of the 45 km nest (the first nest) that allows important aspects of the polar circulation to develop. We find that strong circumpolar easterlies, katabatic flow and transient eddies are all involved in the ventilation of vapor away from the NPRC region. When only the mother domain is active, the model is incapable of resolving these aspects of the circulation. The existence of a sufficiently realistic circulation causes the cloud ice column to become realistic in comparison with observations; and, when the second nest is made active, no further reduction in the ice column is seen. The formation of a realistic circulation in the polar region causes the excessive cloudiness seen in the model to disappear.

Three additional mother domain only runs were performed to test the effects of (1) shorter microphysics time-stepping, (2) smoother polar topography, and (3) lessened dynamical diffusion. None of these tests caused the circulation to be more realistic or reduced the excessive cloudiness. For this crucial season in the annual water cycle, the polar circulation is highly complex, and sufficient spatial resolution appears to be a basic requirement if a realistic simulation of water ice clouds during northern polar summertime (for the right reasons) is desired. Since the activation of the first nest allows the circulation to be resolved, we find that a grid spacing of ~1° is probably sufficient to resolve the crucial dynamics. This study is unable to address the "pole problem" and how it may be involved. Certainly, the cloud scheme used in this study has fewer "degrees of freedom" than a more sophisticated cloud scheme, and it is possible that the sensitivity to spatial resolution seen in this study is somehow related.

Results from this modeling study are consistent with numerous independent observations gathered during the Phoenix mission in 2008. Our modeling suggests that independently observed events (spaced very closely in L_s) are dynamically related. LIDAR observations show that the vertical structure of cloud ice over Phoenix undergoes a rapid change at $L_s = 122°$ (Phoenix sol number 99). Before this date cloud ice had only been observed above ~10 km AGL, while after this date it can be seen very near the ground in the early AM. Just prior to this rapid change in the cloud heights, the linear decrease of the Phoenix surface pressure record is interrupted by a strong low-pressure system that modifies the record over a period of ~2–3 sols (the center is sol 94, or $L_s = 120°$). In the model, a "storm zone" exists on the northern slopes of Alba Patera. This "storm zone" produces a large cyclonic (low-pressure) disturbance, which migrates into the region just to the northeast of Phoenix (just after $L_s = 120°$). In the model, the arrival of this disturbance is followed by a rapid change in cloud heights that is similar to what was observed by the Phoenix LIDAR. Then, after a couple more sols, an annular cloud forms in the early AM model atmosphere. Compared with observations, the simulated annular cloud is of the same size, and appears at a location and time of day that is in very good agreement with the recurring annular cloud described by Cantor et al. (2002) and Malin et al. (2010). Composite MARCI imagery shows that the 2008 appearance of the annular cloud follows the surface pressure excursion by a couple sols, at $L_s = 121.9°$ (Bruce Cantor, personal communication, 2013), forming very closely in L_s to the other observations.

Because of the very close timing seen in both the observations and the model, a dynamical relationship is suspected between the changes in clouds observed by the Phoenix LIDAR, the sizeable excursion observed in the surface pressure record and the appearance of the annular cloud. In both the model and on Mars this all occurs over a short period of ~5 sols. The OSU MMM does not predict the large surface pressure excursion at Phoenix that was observed, although a singular and very strong cyclonic disturbance moves through the region to the east of the lander site with an amplitude that is as large as that in the observations (~1%). In the model, the circulation associated with the surface pressure excursion is dynamically responsible for modifying the spatial distribution of atmospheric water vapor, and this is the primary reason for the formation of an annular cloud. With the proximity of a strong transient disturbance, more vigorous dynamics would be expected to exist, and would likely have a role in the rapid changes seen in modeled clouds over Phoenix. This conclusion is supported through the analysis of imagery in this very specific L_s window (Moores et al., 2010).

With a sizeable signal in the Phoenix surface pressure record, the existence of a strong transient is certain. As evidence of increased dynamical vigor in the local atmosphere, wind speeds (both modeled and observed) are significantly larger due to its existence. The Phoenix LIDAR observed a threefold decrease in the opacity of dust, which would almost certainly mean the formation of larger ice particles that would fall faster and nearer to the ground. It is not completely clear what caused the rapid change in the observed cloud heights above Phoenix, although dynamics related to the proximity of a strong transient disturbance seem to be involved. It is possible that this rapid sequence of events

signifies a seasonal transition, one that is marked with the appearance of the seasonally recurring annular cloud.

Mesoscale modeling has an important role in understanding these issues. With the certainty of a highly complex northern polar summertime circulation, and the importance of this season and region in the annual water cycle, dynamical modeling that is sufficiently realistic for scientific investigation of polar processes requires a renewed consideration of the importance of resolution and its effect on model results. Without a doubt, careful study of the $L_s \sim 120^\circ$ season is crucial as we strive for better simulations of the climate system. The use of "semi-interactive" dust schemes and other creative variants that allow additional freedoms in modeling, while simultaneously maintaining a realistic atmospheric state, are likely to be very useful as our skill level improves. Future efforts with the OSU MMM will include an explicit nucleation phase, where the fallout of ice particles can modify the number density of dust particles, and the dust particle size distribution will be relaxed towards a realistic prescribed distribution. With more complete microphysics, and radiatively active water ice clouds, future efforts will help to refine our understanding of the complex circulation during northern polar summertime.

Appendix A. Supplementary material

Supplementary data associated with this article can be found, in the online version, at http://dx.doi.org/10.1016/j.icarus.2014.04.020.

References

Bottger, H.M., Lewis, S.R., Read, P.L., Forget, F., 2005. The effects of the martian regolith on GCM water cycle simulations. Icarus 177, 174–189. http://dx.doi.org/10.1016/j.icarus.2005.02.024.

Cantor, B., Malin, M., Edgett, K.S., 2002. Multiyear Mars Orbiter Camera (MOC) observations of repeated martian weather phenomena during the northern summer season. J. Geophys. Res. 107 (E3), 5014. http://dx.doi.org/10.1029/2001JE001588.

Daerden, F. et al., 2010. Simulating observed boundary layer clouds on Mars. J. Geophys, Res. 37 (L04203), doi:10.1029/2009GL041523.

Haberle, R.M. et al., 2011. Radiative effects of water ice clouds on the martian seasonal water cycle. In: Fourth International Conference on the Mars Atmosphere: Modeling and Observations, Paris, February 8–11.

Holstein-Rathlou, C. et al., 2010. Winds at the Phoenix landing site. J. Geophys. Res. 115 (E00E18), doi:10.1029/2009JE003411.

Hong, S., Pan, H., 1996. Nonlocal boundary layer vertical diffusion in a medium-range forcast model. Mon. Weather Rev. 124, 2322–2339.

Houben, H., Haberle, R.M., Young, R.E., Zent, A.P., 1997. Modeling the martian seasonal water cycle. J. Geophys. Res. 102 (E4). http://dx.doi.org/10.1029/97JE00046.

Iraci, L.T., Phebus, B.D., Stone, B.M., Colaprete, A., 2010. Water ice cloud formation on Mars is more difficult than presumed: Laboratory studies of ice nucleation on surrogate materials. Icarus 210, 985–991. http://dx.doi.org/10.1016/j.icarus.2010.07.020.

Kahre, M.A., Murphy, J.R., Haberle, R.M., 2006. Modeling the martian dust cycle and surface dust reservoirs with the NASA Ames general circulation model. J. Geophys. Res. 111 (E06008). http://dx.doi.org/10.1029/2005JE002588.

Lemmon, M.T., 2014. Large water ice aerosols in martian north polar clouds. In: Fifth International Conference on the Mars Atmosphere: Modeling and Observations, Oxford, January 13–16.

Lian, Y., Richardson, M.I., Newman, C.E., Lee, C., Toigo, A.D., Mischna, M.A., Campin, J.-M., 2012. The Ashima/MIT mars GCM and argon in the martian atmosphere. Icarus 218 (2), 1043–1070. http://dx.doi.org/10.1016/j.icarus.2012.02.012.

Madeleine, J.-B., Forget, F., Millour, E., Spiga, A., Montmessin, F., Maattanen, A., 2011. The water cycle in the northern polar region of Mars: Improved modeling using the LMD global climate model. In: Fifth Mars Polar Sci. Conf., #6075, Fairbanks, September 12–16.

Madeleine, J.-B., Forget, F., Millour, E., Spiga, A., 2012. The influence of radiatively active water ice clouds on the martian climate. GRL 39 (L23202). http://dx.doi.org/10.1029/2012GL053564.

Malin, M.C., Calvin, W.M., Cantor, B.A., Clancy, R.T., Haberle, R.M., James, P.B., Thomas, P.C., Wolff, M.J., Bell III, J.F., Lee, S.W., 2008. Climate, weather, and north polar observations from the Mars Reconnaissance Orbiter Mars Color Imager. Icarus 194 (2), 501–512. http://dx.doi.org/10.1016/j.icarus.2007.10.016.

Malin, M.C. et al., 2010. An overview of the 1985–2006 Mars Orbiter Camera science investigation. Mars 5, 1–60. http://dx.doi.org/10.1555/mars.2010.0001.

McCleese, D.J. et al., 2007. Mars Climate Sounder: An investigation of thermal and water vapor structure, dust and condensate distributions in the atmosphere, and energy balance of the polar regions. J. Geophys. Res. 112 (E05S06), doi:10.1029/2006JE002790.

Montmessin, F., Forget, F., Rannou, P., Cabane, M., Haberle, R.M., 2004. Origin and role of water ice clouds in the martian water cycle as inferred from a General Circulation model. J. Geophys. Res. 109 (E10004). http://dx.doi.org/10.1029/2004JE002284.

Moores, J.E., Lemmon, M.T., Smith, P.H., Komguem, L., Whiteway, J.A., 2010. Atmospheric dynamics at the Phoenix landing site as seen by the Surface Stereo Imager. JGR 115 (E00E08), doi:10.1029/2009JE003409.

Nelli, S.M., Renno, N.O., Murphy, J.R., Feldman, W.C., Bougher, S.W., 2010. Simulations of atmospheric phenomena at the Phoenix landing site with the Ames General Circulation Model. J. Geophys. Res. 115 (E00E21), doi:10.1029/2010JE003568.

Putzig, N.E., Mellon, M.T., 2007. Apparent thermal inertia and the surface heterogeneity of Mars. Icarus 191, 68–94. http://dx.doi.org/10.1016/j.icarus.2007.05.013.

Richardson, M.I., Wilson, R.J., 2002. Investigation of the nature and stability of the martian seasonal water cycle with a general circulation model. J. Geophys. Res. 107 (E5). http://dx.doi.org/10.1029/2001JE001536.

Smith, M.D., 2002. The annual cycle of water vapor on Mars as observed by the Thermal Emission Spectrometer. J. Geophys. Res. 107 (E11). http://dx.doi.org/10.1029/2001JE001522.

Smith, M.D., Conrath, B.J., Christensen, P.R., 2001. Thermal Emission Spectrometer results: Mars atmospheric thermal structure and aerosol distribution. J. Geophys. Res. 106 (E10), 23929–23945. http://dx.doi.org/10.1029/2000JE001321.

Tamppari, L.K. et al., 2010. Phoenix and MRO coordinated atmospheric measurements, J. Geophys. Res. 115 (E00E17), doi:10.1029/2009JE003415.

Taylor, P.A. et al., 2010. On pressure measurement and seasonal pressure variations during the Phoenix mission. J. Geophys. Res. 115 (E00E15), doi:10.1029/2009JE003422.

Titus, T., 2005. Mars polar cap edges tracked over 3 full Mars years. 36th LPSC, League City, TX, #1993.

Tyler Jr., D., Barnes, J.R., 2005. A mesoscale model study of summertime atmospheric circulations in the North Polar Region of Mars. J. Geophys. Res. 110 (E06007). http://dx.doi.org/10.1029/2004JE002356.

Tyler, D. Jr., Barnes, J.R., 2011. Atmospheric mesoscale modeling of water and clouds in northern summer. In: 5th Mars Polar Sci. Conf., Fairbanks, AK, #6049.

Tyler Jr., D., Barnes, J.R., 2013. Mesoscale modeling of the circulation in the Gale Crater region: An investigation into the complex forcing of convective boundary layer depths. Mars 8, 58–77. http://dx.doi.org/10.1555/mars.2013.0003.

Tyler Jr., D., Barnes, J.R., Haberle, R.M., 2002. Simulation of surface meteorology at the Pathfinder and VL1 sites using a Mars mesoscale model. J. Geophys. Res. 107 (5018), doi:10.1029/2001JE001618.

Tyler Jr., D., Barnes, J.R., Skyllingstad, E.D., 2008. Mesoscale and large-eddy simulation model studies of the martian atmosphere in support of Phoenix. J. Geophys. Res. 113 (E00A12). http://dx.doi.org/10.1029/2007JE003012.

Whiteway, J.A. et al., 2009. Mars water ice clouds and precipitation. Science 325, 68–70. http://dx.doi.org/10.1126/science.1172344.